iScience

CellPress
OPEN ACCESS

Article

Cystine-cored diphenylalanine appended peptide-based self-assembled fluorescent nanostructures direct redox-responsive drug delivery

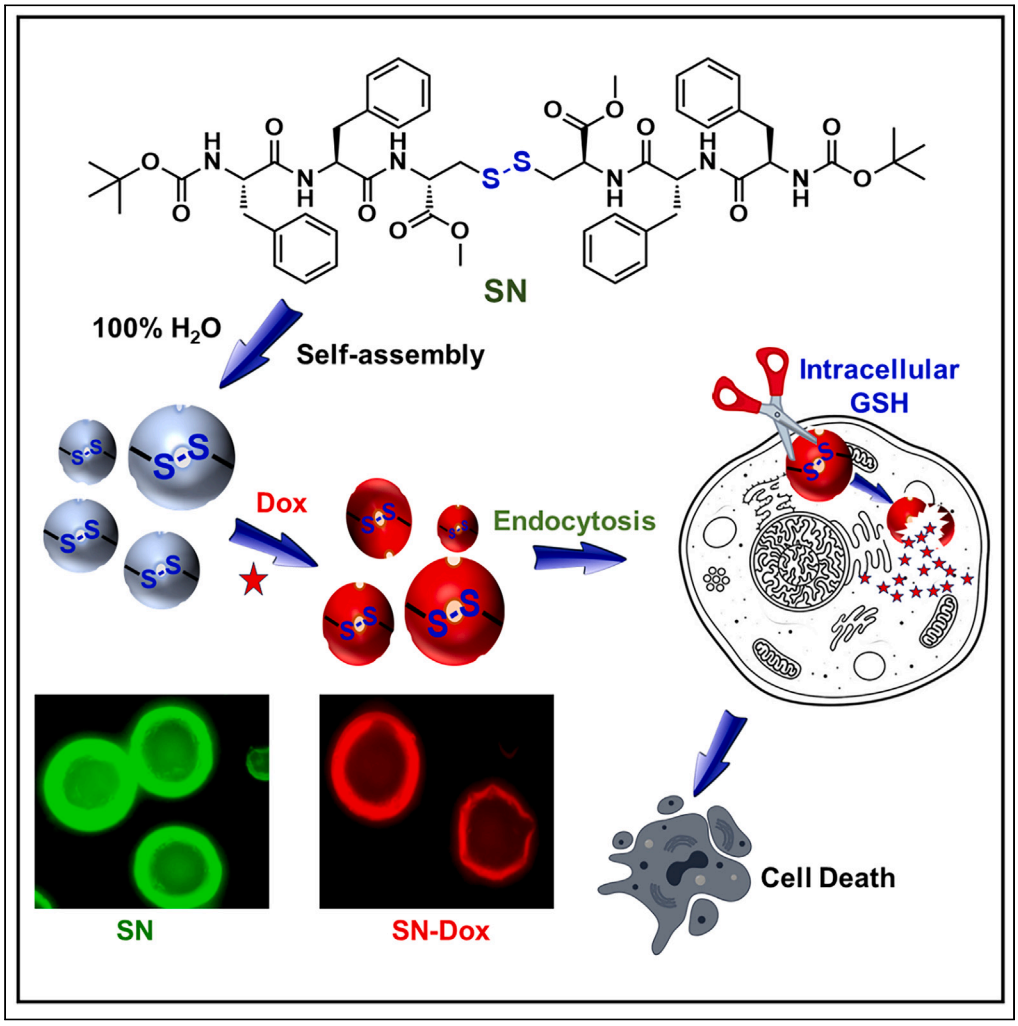

Suman Nayak, Kiran Das, Subramaniyam Sivagnanam, ..., Dinesh Kumar, Biswanath Maity, Priyadip Das

bmaity28@gmail.com (B.M.)
priyadipcsmcri@gmail.com (P.D.)

Highlights

Redox-responsive hollow spheres enable intracellular site-specific drug delivery

Elevated glutathione levels in cancer cells trigger the drug release.

Fluorescent SN-Dox offers real-time intracellular monitoring of drug release.

SN-Dox exhibits lower effective concentration for breast cancer cell viability.

Nayak et al., iScience 27, 109523
April 19, 2024
https://doi.org/10.1016/j.isci.2024.109523

iScience

CellPress
OPEN ACCESS

Article

Cystine-cored diphenylalanine appended peptide-based self-assembled fluorescent nanostructures direct redox-responsive drug delivery

Suman Nayak,[1,5] Kiran Das,[2,5] Subramaniyam Sivagnanam,[1,5] Shyamvarnan Baskar,[1] Adele Stewart,[4] Dinesh Kumar,[3] Biswanath Maity,[2,*] and Priyadip Das[1,6,*]

SUMMARY

Fabrication of stimuli-responsive superstructure capable of delivering chemotherapeutics directly to the cancer cell by sparing healthy cells is crucial. Herein, we developed redox-responsive hollow spherical assemblies through self-assembly of disulfide-linked cysteine-diphenylalanine (SN). These fluorescent hollow spheres display intrinsic green fluorescence, are proteolytically stable and biocompatible, and allow for real-time monitoring of their intracellular entry. The disulfide bond facilitates selective degradation in the presence of high glutathione (GSH) concentrations, prevalent in cancer cells. We achieved efficient encapsulation (68.72%) of the anticancer drug doxorubicin (Dox) and demonstrated GSH-dependent, redox-responsive drug release within cancerous cells. SN-Dox exhibited a 20-fold lower effective concentration (2.5 μM) for compromising breast cancer cell viability compared to non-malignant cells (50 μM). The ability of SN-Dox to initiate DNA damage signaling and trigger apoptosis was comparable to that of the unencapsulated drug. Our findings highlight the potential of SN for creating site-specific drug delivery vehicles for sustained therapeutic release.

INTRODUCTION

Advancements in the design and generation of efficient drug delivery systems have been driven by a demand for improved drug efficacy and specificity with the goal of minimizing adverse side effects particularly for drugs like cancer chemotherapeutics with extremely narrow therapeutic indices.[1–6] The clinical utility of nanomedicines comprising chemotherapeutic drugs encapsulated in nanoparticle-based drug delivery systems (NDDSs) such as liposomes or dendrimers demonstrates the feasibility of this approach.[7–12] However, available NDDSs materials suffer from several limitations including poor intracellular uptake and ineffectual drug release at the disease site. In addition, the generation of a successful NDDSs-based nanomedicine also requires optimization of circulation time, organ accumulation, and binding capacity at a target cell. Notably, peptide-based self-assembled superstructures remain of particular interest due to their unmatched biocompatibility, tunable properties, biodegradability, natural propensity for cellular targeting, and ability to release encapsulated drug molecules in a controlled manner.[13–15] The ability to control both the location and temporal pattern of drug release remains an attractive prospect in the development of nanomedicines. To this end, stimulus-responsive drug delivery platforms have been generated[16,17] that allow for controlled drug release in response to external (e.g., light, ultrasound, and magnetic field[17–20]) or internal (e.g., enzymes, temperature, pH, and redox potential[21–24]) stimuli. In theory, such NDDSs would both improve drug efficacy by facilitating highly specific targeting of drug to the desired site and, simultaneously, decrease off-target side effects.[25]

Glutathione (GSH), a thiolated tripeptide, is the most abundant thiol in mammalian and eukaryotic cells and plays a crucial role in cellular defense against toxins and free radicals as well as cell proliferation and survival.[26–28] Alterations in GSH levels are associated with several human diseases including cancer, liver disease, acquired immunodeficiency syndrome (AIDS), and Alzheimer's disease.[29] Cancer cells, for instance, often have a more reducing intracellular environment due to the presence of higher levels (2–10 mM) of reducing agents such as GSH intracellularly.[24,30] Excess GSH in malignant cells is also associated with tumor progression and metastasis.[31] As GSH catalyzes the cleavage or reduction of disulfide bonds, the aberrant accumulation of GSH in cancer cells raises the possibility that a GSH-sensitive, disulfide bond-functionalized drug carrier might allow for selective accumulation of encapsulated drug in malignant cells while sparing healthy tissues.[24] Indeed, Ahn et al. recently designed and synthesized a reversibly crosslinked block copolymer (PEG-PCL) linked through a tripeptide

[1]Department of Chemistry, SRM Institute of Science and Technology, SRM Nagar, Potheri, Kattankulathur, Tamil Nadu 603203, India
[2]Department of Systems Biology, Centre of Biomedical Research (CBMR), SGPGI campus, Raebareli Road, Lucknow, Uttar Pradesh 226014, India
[3]Department of Advanced Spectroscopy and Imaging, Centre of Biomedical Research (CBMR), SGPGI campus, Raebareli Road, Lucknow, Uttar Pradesh 226014, India
[4]Department of Biomedical Science, Charles E. Schmidt College of Medicine, Florida Atlantic University, Jupiter, FL 33458, USA
[5]These authors contributed equally
[6]Lead contact
*Correspondence: bmaity28@gmail.com (B.M.), priyadipcsmcri@gmail.com (P.D.)
https://doi.org/10.1016/j.isci.2024.109523

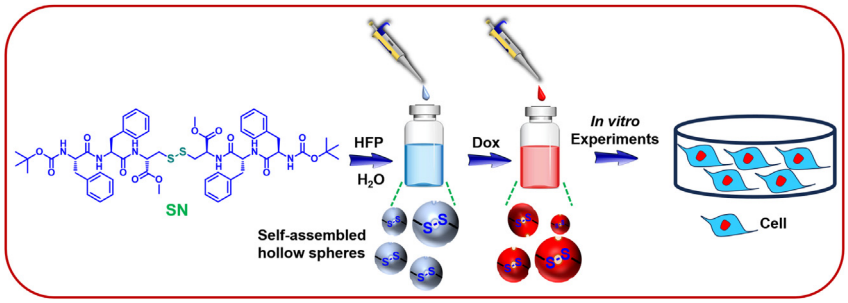

Figure 1. Schematic representation of formation of SN-based self-assembled hollow spheres, Dox encapsulation, and their application in drug delivery

with three cysteine residues (PEG-Cys3-PCL). The biodegradable micelles self-assembled from PEG-Cys3-PCL displayed considerable stability and allowed for sustained release (24 h) of the encapsulated chemotherapeutic drug doxorubicin (Dox) from these micellar assemblies. Notably, the introduction of 1mM DTT (dithiothreitol) triggered a rapid and substantial burst release of encapsulated Dox due to the reduction of disulfide linkage by DTT.[32] This study provided initial evidence that cysteine incorporation into the peptide backbone of a NDDSs allowed for redox-dependent drug release. However, the authors failed to investigate whether this approach would allow for cancer cell-specific drug delivery in an intact biological system.

With the aim to develop a disulfide-functionalized short peptide-based self-assembled super structures as a potential drug carrier, we have designed and synthesized an L-Cystine-cored N-Boc diphenylalanine-appended tetra peptide Boc-Phe-Phe-Cys-Phe-Phe-Boc (SN) which self-assembles into hollow spherical structures in highly polar 100% aqueous medium with characteristic green fluorescence. These disulfide (-S-S-)-functionalized assemblies exhibited not only appreciable drug encapsulation capacity but also redox-responsive release of encapsulated drug through GSH-triggered disulfide bond cleavage (Figure 1). These SN-based nanostructures are biocompatible and permitted the transportation and redox-responsive release of Dox in cancer cell with elevated GSH levels resulting in rapid and robust cell death. Together these data demonstrate the potential clinical utility of SN-based nanomedicines in the site-specific delivery of cancer chemotherapy.

RESULTS AND DISCUSSION

Synthesis of SN

In this present study, we have designed and synthesized a disulfide-functionalized peptide SN in which two diphenylalanine (FF) units are linked through a cystine moiety (Scheme 1). This cystine cored tetrapeptide SN was synthesized by simple conventional solution phase peptide synthesis method using N,N′′- Dicyclohexylcarbodiimide (DCC)/1-Hydroxy benzotriazole (HOBt) as coupling reagents. Scheme 1 shows the synthesis and chemical structure of the final tetrapeptide SN. The detailed synthetic procedures are provided in the supplemental information (Schemes S1 and S2). Standard characterization methods were employed to characterize all the synthesized intermediates and final tetrapeptide.

Self-assembly of SN in 100% aqueous medium

The rational design of this newly synthesized peptide SN incorporates three crucial elements. (i) First, the aromatic dipeptide moiety in the peptide backbone (FF) directs self-aggregation through π-π stacking interactions and is also predicted to interact with the aromatic moiety of the chemotherapeutic drug Dox, which will improve encapsulation efficiency (EE) and loading capacity (LC). (ii) The presence of N-terminal bis-*tert*-butyloxycarbonyl (Boc) group at the two ends of this tetrapeptide controls the magnitude of solvophobic interactions during self-assembly and consecutively reduces the surface energy of the fabricated assembly. (iii) Of the possible cleavable linkers, disulfide (-S-S-) bonds are very attractive because they are stable in most blood pools but are effectively cleaved by cellular thiols such as GSH and thioredoxin, which are usually present at elevated level in tumors. In addition, attaching a chromogenic moiety with a disulfide bond significantly alters the emission intensity or shifts the emission maximum upon cleavage due to the perturbations in the intramolecular charge transfer (ICT) process. This is extremely helpful in the design of theranostics, chemical entities that combine therapeutic effects and imaging capability within a single molecular system.

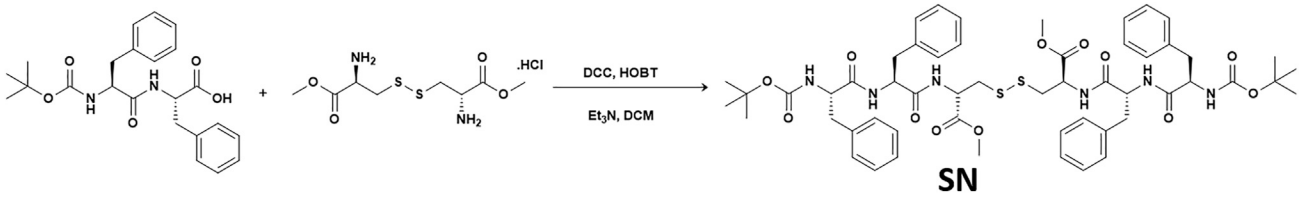

Scheme 1. Synthetic methodology adopted for the synthesis of SN

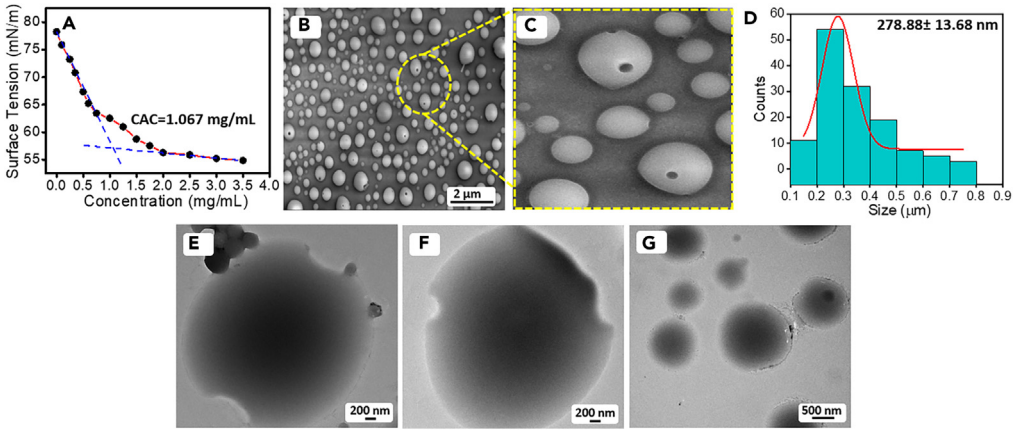

Figure 2. Morphological characterization

(A) Determination of CAC for the self-assembly of SN. Morphological characterization of the self-assembled structures formed by SN: (B and C) HR-SEM and (D) size distribution of the hollow spheres obtained from HR-SEM micrograph and (E–G) HR-TEM micrographs of the self-assembled hollow spherical structures formed by SN in 100% aqueous medium.

We measured the surface tension of SN solution at different concentrations and successfully determined the critical aggregation concentration (CAC) from the plot of surface tension vs. concentration. Initially, there was a steady decrease of surface tension value with increasing concentration of SN that then reached a plateau. The intersection between the regression straight lines corresponds to the linear concentration-dependent and independent regions, yielding a CAC value of 1.067 mg mL^{-1} (Figure 2A).

Next, we studied the self-assembly properties of this newly synthesized disulfide-functionalized peptide SN in highly polar 100% aqueous medium. For this purpose, we dissolved the peptide in 1,1,1,3,3,3-hexafluoro-2-propanol (HFP) with an initial concentration of 100 mg mL^{-1}. This stock solution was further diluted with distilled water to attain the final concentration of 2 mg mL^{-1} and then incubated at room temperature for 24 h. Polar solvents like water typically allow for the self-assembly of peptide-based monomeric building blocks into well-ordered assemblies.[33] After incubation, 20 μL of the self-assembled solution was drop casted on a clean glass coverslip, dried at room temperature, and dried by vacuum. High-resolution scanning electron microscopy (HR-SEM) analysis revealed that SN self-assemble into well-ordered hollow spheres into 100% aqueous medium (Figures 2B and 2C). High-resolution transmission electron microscopy (HR-TEM) analysis further confirmed that the SN self-assemble into spherical assembly with hollow[34,35] nature and not droplets or elliptical structures (Figures 2E–2G).[36–39]

Based on the structural conformation of SN, the self-assembly process in mainly triggered by the π-π stacking interactions among the aromatic dipeptide residues diphenylalanine (FF) and intermolecular H-bonding associated with the amide groups of the peptide backbone. In addition to these non-covalent interactions, the aromatic moieties of the diphenylalanine unit and the protected N-terminal Boc groups in the SN provide substantial hydrophobic interactions in a highly polar medium like water and drive the self-assembly process and tune the morphology, shape, and size of the self-assembled structure. In highly polar 100% aqueous medium, it can be anticipated that the hydrophobic FF moieties and N-terminal Boc units would undergo more compact folding to protect the aromatic moieties from hydrophobic interactions and, consequently, minimize the surface energy of the self-assembled structures. In 100% aqueous medium the disulfide-functionalized peptide SN, with two aromatic diphenylalanine (FF) moieties, self-assemble into well-ordered spherical structures with hollow nature consistent with the prior reports.[33,40,41] The average size of the SN-based hollow spherical assembly obtained from HR-SEM micrographs (Figure 2D) is 278.88 ± 13.68 nm, which is in well agreement with the average size (~248.15 ± 4.87 nm) obtained from dynamic light scattering (DLS) (Figure S4).

Computer-aided design (CAD) of SN peptide-based hollow spherical structures

Further, we attempted to create a possible model for self-assembled 3D hollow structure of SN peptide in an HFP/water solvent system. The 3D molecular structure of the SN peptide was generated using the CHEM3D module of CHEMDRAW software and further energy minimized in HFP solvent using YASARA software (Figure S5 of supplemental information). The energy-minimized 3D structure of SN peptide was used for predicting possible peptide-peptide interactions using the VINA docking method.[42] The various possible models of dimeric SN peptide are shown in Figure S5. Of the models generated, the third model with explicit aromatic interactions and head/tail geometry similar to fatty acid molecules forming a lipid bilayer was selected to build a bilayer model with energy minimized in an explicit water solvent. Subsequently, the energy-minimized structure of SN dipeptide was used to model the hollow spherical structure as shown in Figure 3.

Fourier transform infrared (FTIR) spectroscopy

We have also carried out the Fourier transform infrared (FTIR) analysis to gain insight about the secondary structural conformation of the SN-based spherical assembly. The amide-I region of the recorded FTIR spectrum of SN-based self-assembled structure was deconvoluted using a

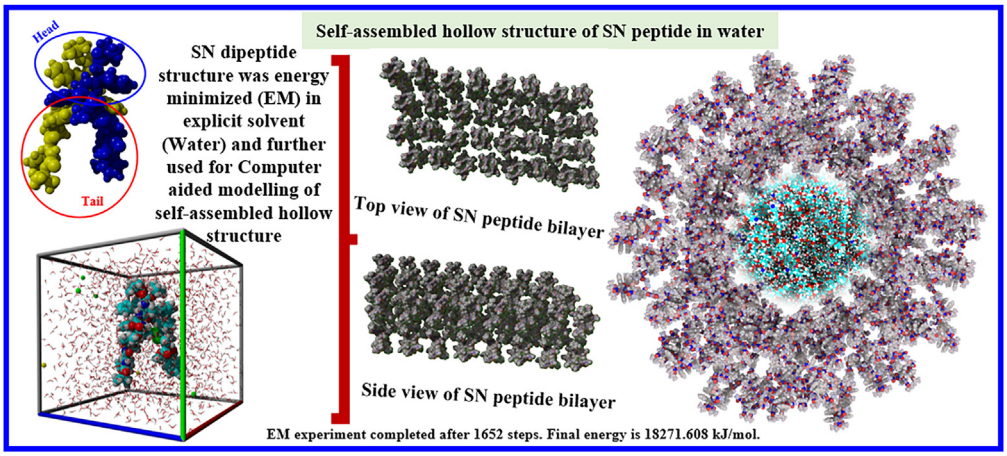

Figure 3. Computer-aided design (CAD) of SN peptide-based hollow spherical structures

The dimeric SN peptide structure generated using VINA molecular docking experiments and energy minimized in explicit water solvent using YASARA software. The arrangement of two SN peptide molecules exhibited preferential attraction of the aromatic groups. The head and tail segments of SN dipeptide (as depicted) with slight structural asymmetry may lead to the formation of self-assembled hollow similar to the formation of liposomal vesicles from phospholipid (fatty acid) chains.

Gaussian function. This deconvoluted FTIR spectra of the SN-based spherical assembly exhibited two major peaks at 1,616 cm^{-1} and 1,642 cm^{-1} and one minor peak at 1,695 cm^{-1} (Figure 4A) in the amide-I region. The peak at 1,616 cm^{-1} indicates the presence of an extended hydrated structure.[43] Another major peak at 1,642 cm^{-1} and the high-frequency minor band at 1,695 cm^{-1} confirmed the presence of an anti-parallel β sheet conformation.[44,45] The secondary structure of SN was further confirmed by circular dichroism (CD) spectroscopy. The CD spectra of SN displayed a characteristic positive peak at ~197 nm and a negative peak at ~217 nm (Figure S6), which clearly indicates the presence of an antiparallel β sheet confirmation.[46]

Optical properties of the SN-based hallow spherical assembly

Following the morphological analysis, we further recorded the ultraviolet-visible (UV-vis) absorption spectra of SN in both monomeric and self-assembled states in 100% aqueous medium. UV-vis absorption spectra of monomeric SN displayed an absorption peak at 270 nm (Figure 4B),

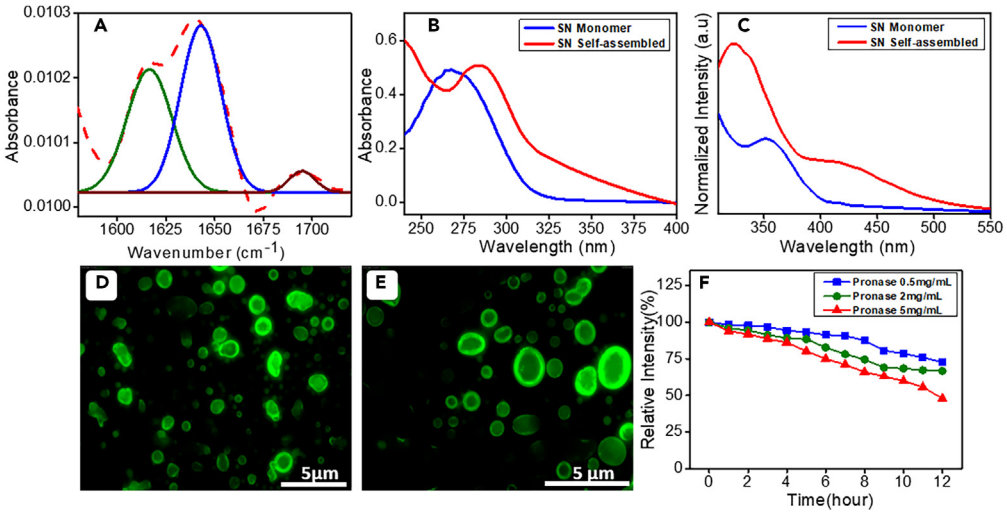

Figure 4. FTIR analysis, optical properties, and proteolytic stability of SN

(A) Deconvoluted FTIR spectrum of SN-based self-assembled hollow spheres.

(B) UV-vis absorption spectra of SN both in monomeric (blue) and self-assembled state (red).

(C) Steady-state emission spectra of SN in both monomeric (blue) and self-assembled state (red).

(D and E) Fluorescence microscopy images SN-based self-assembled hollow spherical assembly.

(F) Protease stability analysis of SN (2 mg mL^{-1}, λ_{Mon} = 420 nm) using different concentrations of pronase from *Streptomyces griseus*.

while in self-assembled state the absorption maximum was redshifted and appeared at 285 nm (Figure 4B). This absorption peak could be ascribed to the aromatic moiety based π-π^* transition, where the relatively weaker n-π^* transition is overlapped with the strong π-π^* transition.[13] Highly polar medium like water affects the molecular order during the self-assembly process and stabilizes the lowest unoccupied molecular orbital (LUMO) associated with the aromatic based π-π^* transition and n-π^* transition, which is responsible for the effective redshift of the characteristic absorption maximum of SN in the self-assembled state. Polar solvents, due to their inherent properties, tend to stabilize the LUMO by lowering its energy, consequently leading to a notable decrease in the energies of the corresponding electronic transitions and a subsequent redshift of the absorption band.[47] For a better understanding of SN-based molecular association, we have recorded the steady-state emission spectra of SN in both monomeric and self-assembled state in 100% aqueous medium. The steady-state emission spectra of monomeric SN exhibited a characteristic emission maximum at 356 nm (Figure 4C). In the self-assembled state, a new emission maximum at 420 nm appeared in the visible region along with the characteristic monomeric emission maximum of SN (Figure 4C) at 365 nm. It was previously reported that monomeric non-fluorescent peptide molecules form into well-ordered super structures with inherent fluorescent properties.[48,49] However, occasionally the formation of unwanted excimers and exciplexes during association quenched the inherent emission property of the monomeric building block, a process known as aggregation caused quenching.[50] The appearance of a broad new emission peak in the visible region of the spectrum for the self-assembled state of SN is due to a distinct process termed aggregation-induced emission (AIE)[50–52] which allows non-emissive monomeric building blocks of SN self-assemble into fluorescent hollow spherical assemblies. Therefore, the emission spectrum of SN in the self-assembled state (Figure 4C) displayed two different emission peaks. The lower wavelength peak at 365 nm corresponds to non-emissive monomeric state of SN, and the emission peak in the visible region at 420 nm corresponds to the emissive self-assembled state of SN.

Fluorescence microscopy analysis of SN-based hollow spherical assembly

The characteristic fluorescence property of the SN-based spherical assembly was further confirmed by fluorescence microscopy. Figures 4D and 4E show the inherent green fluorescence for the hollow spherical assembly generated/fabricated from SN. The calculated quantum yield (Φ) of the SN-based spherical assembly was found to be 0.72%. We have also investigated the proteolytic stability of these SN-based hollow spheres using the peptidase enzyme pronase derived from *Streptomyces griseus*. This pronase enzyme comprises five serine proteases, two endopeptidases, two leucine aminopeptidases, and one carboxypeptidase (exopeptidase) and effectively hydrolyzes both C and N termini-based peptide bonds.[53] In order to inspect the proteolytic stability of the SN-based hollow spherical assembly, we incubated this SN-based superstructures with pronase enzyme at varying concentrations ranging from 0.5 to 5.0 mg mL^{-1} in phosphate-buffered saline (PBS) at 25°C. After that, we monitored the emission intensity at a specific wavelength (420 nm) at 1 h intervals over a period of 12 h. There was steady fall of emission intensity with increasing concentration of pronase as well as time (Figure 4F). This diminution in the emission intensity was due to the hydrolysis of the peptide bonds within SN by pronase enzyme resulting in a decrease in the concentration of the self-assembled SN-based hollow spherical assembly. Figure 4F clearly illustrates that a moderately high concentration of pronase (5 mg mL^{-1}) and long incubation time (12 h) were necessary to reduce the emission intensity of the self-assembled SN-based spherical assembly below 50%. This result emphasizes the remarkable proteolytic stability exhibited by the SN-based hollow spherical assemblies and confirms their resilience to enzymatic degradation. Finally, we recorded the emission intensity of the self-assembled SN in an aqueous solution of different pH ranging from 2 to 12. Results displayed that at a pH range between 4 and 8 the emission intensities were comparatively high and maximum at physiological pH 7, ideal for biomedical applications (Figure 5A).

Morphological analysis of SN-based self-assembled hollow spherical assembly after Dox encapsulation

In order to examine the potential utility of these SN-based hollow spherical assembly as a possible redox-responsive drug delivery vehicle, we investigated their ability to deliver Dox into cancer cells. To this end, we first performed the self-assembly of SN in 100% aqueous medium in presence of Dox. This process produced the fluorescent Dox-encapsulated hollow sphere, SN-Dox. Fluorescence microscopy analysis demonstrated the successful encapsulation of fluorescent Dox into the hollow sphere (Figures 5B and 5C). The calculated EE and LC were 68.72% and 18.65%, respectively (see STAR Methods). Morphology and the average size of the SN-based hollow spherical assembly after the Dox incorporation (SN-Dox) were also confirmed by HR-SEM analysis. HR-SEM analysis clearly shows the hollow spherical morphology of the SN-Dox (Figures 5D and 5E). The average size of the SN-Dox-obtained HR-SEM micrographs is $\sim 291.63 \pm 1.77$ nm, higher than SN without Dox (Figure 5F). The increase in the average size of the SN-Dox clearly suggests the successful incorporation of the Dox molecules within the hollow spherical assembly.

Redox-responsive properties of SN

The disulfide bonds (-S-S-) undergo a reductive cleavage reaction in the presence of cellular free thiols such as GSH.[54] Next, we examine the redox-responsive behavior and associated drug release capability of SN-Dox in presence of reduced GSH (Figure 5G), whose levels are at least 4-fold higher in glycolytic cancer cells as compared to non-malignant cells.[55] First, we recorded the emission spectra of self-assembled SN in the presence of 1 mM and 5 mM GSH over a period of 30 h (1 h interval). A gradual decrease of the emission intensity of self-assembled SN was observed in the presence of both 1 mM and 5 mM GSH with increase of time (Figures 6A and 6B). The fall in emission intensity was much less in presence of 1 mM of GSH compared to the decrement of emission intensity with 5 mM GSH., which further confirmed the stability of the SN-based hollow spherical assembly in lower concentration of GSH (1 mM). We then recorded the steady-state emission spectra of self-assembled SN in presence of varying concentrations of GSH ranging from 0 to 10 mM Figures 6C and 6D indicate that the emission intensity at 420 nm of self-assembled SN is gradually decreased with increasing concentration of GSH. This diminution in the emission intensity at 420 nm confirmed

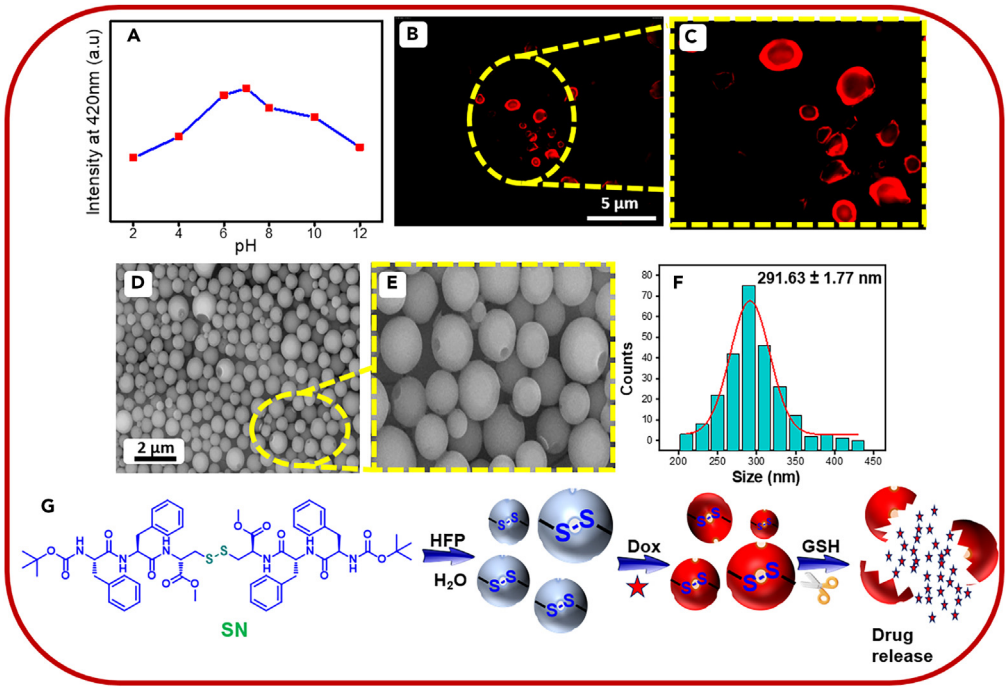

Figure 5. pH-dependent emission and morphological analysis of SN-Dox

(A) Emission intensity of SN in the self-assembled state with varying pH (λ_{Mon} = 420 nm).

(B and C) Fluorescence microscopy images of Doxorubicin (Dox)-encapsulated hollow spherical assemblies generated by SN self-assembly.

(D and E) HR-SEM micrographs of the self-assembled hollow spherical structures formed by SN-Dox in 100% aqueous medium.

(F) Size distribution of the hollow spheres obtained from HR-SEM micrograph of SN-Dox.

(G) Schematic representation of GSH-induced encapsulated Dox release from the hollow spherical assembly.

the GSH mediated disintegration of disulfide linkage present in the SN-based self-assembled structure resulting in the collapse or disintegration of the hollow spherical assembly. Furthermore, the GSH-mediated redox-responsive behavior of Dox-encapsulated SN-based superstructures (SN-Dox) was also examined in presence of varying concentrations of GSH (0–10 mM) at 1 h intervals over a period of 30 h. In presence of

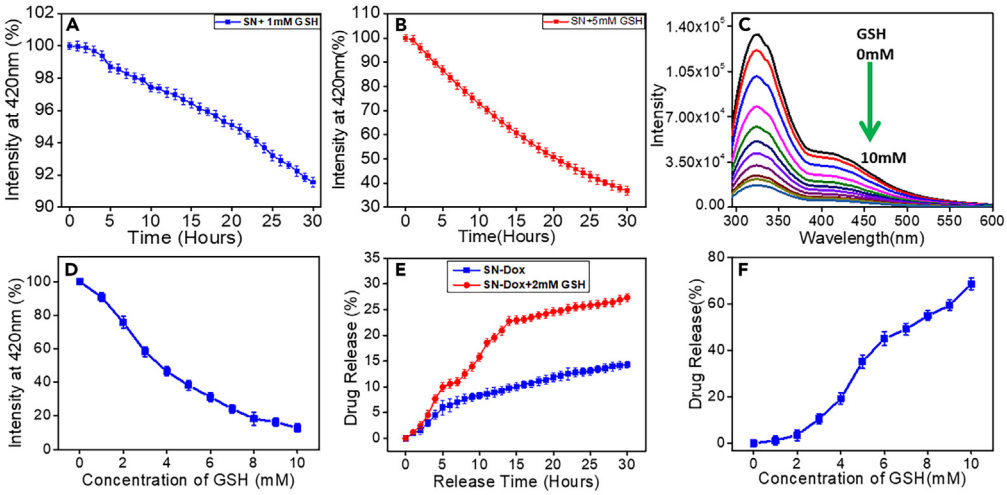

Figure 6. Redox-responsive nature of SN

Emission spectra of self-assembled SN with time in the presence of (A) 1 mM and (B) 5 mM GSH.

(C and D) Emission spectra of self-assembled SN in the presence of different concentrations of GSH varying from 0 to 10 mM, incubation time: 30 h.

(E) Plot of percentage (%) of drug release from the drug-encapsulated self-assembled SN with time in the absence of GSH (blue) and in the presence of 2 mM GSH (red).

(F) Release profile of Dox-loaded SN-based hollow spherical structures in the presence 0–10 mM GSH (λ_{Mon}: 590 nm; λ_{Ext}: 490 nm), incubation time: 30 h.

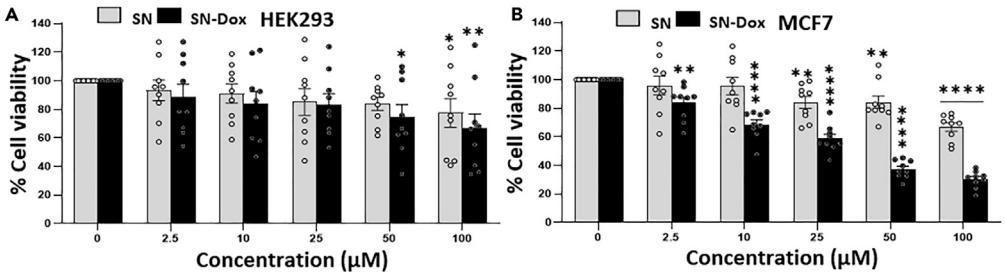

Figure 7. Cytotoxicity and incorporation of the compounds SN and SN-Dox in cell

The cellular toxicity was measured by MTT assay following incubation with various concentrations of SN, and SN-Dox at 36 hrs (A) The survival of human embryonic kidney HEK293 cells.

(B) Cytotoxicity of breast cancer cell MCF7. All results are presented as means + S.E. of multiple experiments (n=9, *p<0.05; **p<0.01, ***p<0.001, ****p<0.0001 compared to untreated control group).

2 mM of GSH, there was a gradual increase in the characteristic emission intensity of Dox (λ_{Mon} = 590 nm) over a period of 30 h and the extent of the Dox release was limited to 27% (Figure 6E). This gradual increase in the emission intensity suggests the sustained release of encapsulated Dox from the hollow spheres due to the GSH-triggered reductive cleavage of disulfide functionality present in the SN backbone. On the other hand, in absence of GSH the extent of the Dox release from the hollow spheres after 30 h was only 12% (Figure 6E). These results confirmed a considerable reduction of premature drug leakage under physiological conditions in the absence of excess GSH. We have also generated the drug release profile of SN-Dox in presence of varying concentration of GSH (0–10 mM) after a 30 h incubation time. Figure 6F shows incremental Dox release with increasing concentration of GSH, and a maximum Dox release of 68% was observed after 30 h. This result shows that GSH-induced reductive cleavage of the disulfide bond is solely responsible for the release of encapsulated Dox from SN-based hollow spheres. Compared to other redox-responsive polymeric drug delivery systems, the rate of Dox release from the SN-based hollow spheres was comparatively slower,[56,57] highlighting the potential of SN-based hollow spheres as a sustained drug delivery vehicle.

In vitro experiments

MTT assay

The cellular toxicity was checked on the treatment of SN and SN-Dox compounds in human embryonic kidney HEK293 cells (Figure 7A) and the human cardiomyocytes cell line AC-16 (Figure S7A). In non-malignant cells (HEK293 and AC-16), both the SN compound and SN-Dox trigger cell loss only at high concentrations of 100 and 50 μM, respectively (Figures 7A and S7A). However, in cancerous cells (MCF7 and MDAMB231 cells), SN-Dox treatment resulted in significant loss of cell viability in concentrations as low as 2.5 μM (Figures 7B and S7B). These data show that SN facilitates more efficient delivery of cytotoxic Dox into cancerous cells, which are known to contain higher levels of intracellular GSH. Next, we confirmed the bioactivity of SN-Dox in both MCF7 and MDAMB231 breast cancer cells comparing SN-Dox to the unencapsulated drug as a positive control (Figure 8A). As expected, Dox and SN-Dox both triggered a similar degree of apoptosis in both cancer cell lines (Figure 8B). Dox is known to trigger cell death via the intrinsic mitochondrial apoptosis pathway which can be initiated in response to oxidative stress or DNA damage. Both Dox and SN-Dox lead to loss of mitochondrial membrane potential ($\Delta\Psi_M$) in breast cancer cells

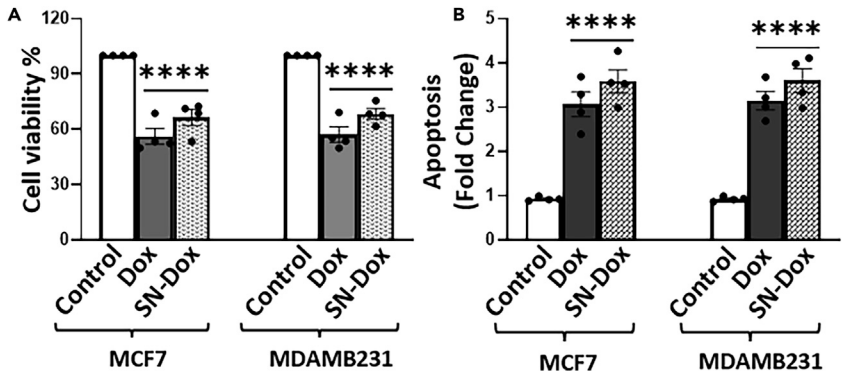

Figure 8. The apoptotic cell death was promoted by SN-encapsulated Dox (SN-Dox)

(A) MTT assay was used to measure the cellular toxicity of cancer cells (MCF7 and MDAMB231) after incubation with Dox, and SN-Dox (1 μM) at 36 hrs. Data are shown as means + S.E. (n=4, **p<0.01, ****p<0.0001 compared with control received less than 0.1% DMSO).

(B) Apoptosis was measured as the rise in fold increase in enrichment factor by formation of the cytoplasmic histones coupled DNA fragments.

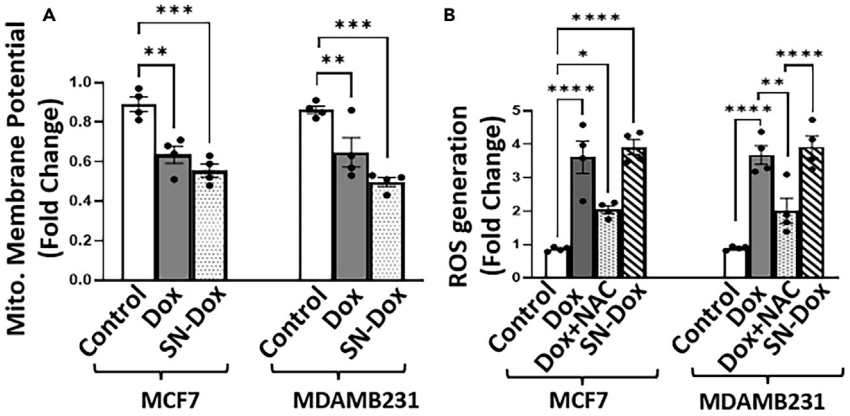

Figure 9. DNA damage response was triggered by SN-Dox in the MCF7 and MDAMB231 cancer cells

(A) Loss of mitochondrial membrane potential (Dy_m) and (B) generation of ROS in MCF7 and MDAMB231 cancer cells were induced by Dox and SN-Dox (1 μM). The ROS generation was measured by using CM-H2DCFDA at 24 hrs. All results are expressed as means + S.E. (n=4, *p<0.05, **p<0.01, ***p<0.001, ****<0.0001 compared to control group with vehicle only).

(Figure 9A), a critical initial step in mitochondrial-dependent cell death signaling. Similarly, the ability of Dox and SN-Dox to increase intracellular reactive oxygen species (ROS) levels was comparable (Figure 9B), a phenomenon sensitive to ROS scavenging with the GSH donor N-acetyl cysteine (NAC). These data provided initial evidence that Dox encapsulation with SN does not compromise the cell killing action of the drug. In addition, these data suggest that SN is capable of shuttling Dox into cells where it is then released.

Cell diffusion assay

Consistent with the cell killing actions of SN-Dox, we noted that Dox and SN-Dox, but not SN alone, resulted in DNA damage in MCF7 cells (Figure 10A) consistent with our ability to monitor uptake of SN-Dox into these cells via fluorescence microscopy (Figure 10B). The human breast carcinoma epithelial cell MCF7 was treated with 100 nM of SN-Dox for a period of 1 h allowing for visualization of the synthesized SN compound emitting bright green fluorescence whereas the red fluorescence signal is from Dox (Figure 10B), and, when the treatment duration was increased (i.e., 8 h), the green-colored fluorescence intensity of SN compound was faded probably due to the breakdown of the compound (SN) and red colored Dox was released to the nucleus (Figure S8).

DNA fragmentation assay

Dox-driven DNA damage triggers several key intracellular signaling cascades. First, the kinase Ataxia-Telangiectasia mutated (ATM) is recruited to the site of double-strand DNA breaks where it phosphorylates histone H2AX (γH2AX). ATM also activates the tumor suppressor p53 responsible for up-regulating pro-apoptotic proteins such as p53 upregulated modulator of apoptosis (PUMA) and Bax and

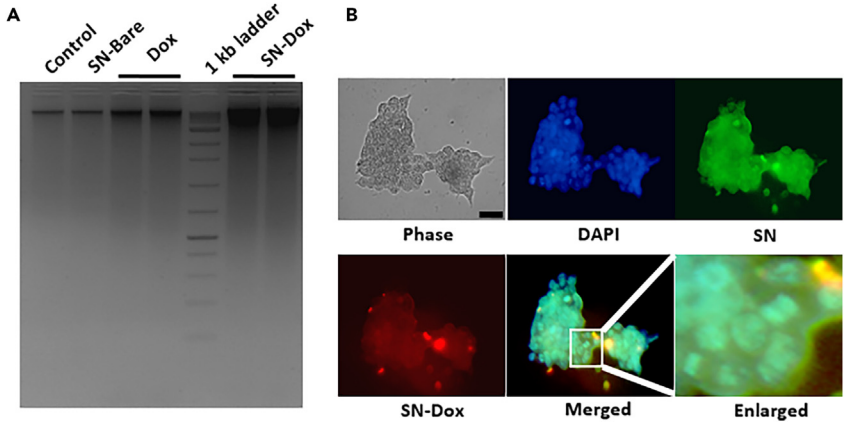

Figure 10. Incorporation of SN and SN-Dox delivery into MCF7 cells

(A) DNA damage can be visualized in Dox- and SN-Dox-treated cells but not in SN alone using DNA laddering and (B) *In vitro* fluorescence imaging of MCF7 cells with SN and SN-Dox (100 nM). The green color represents the fluorescence by SN compound whereas the red color shows the signal from doxorubicin (scale bar, 100 μm).

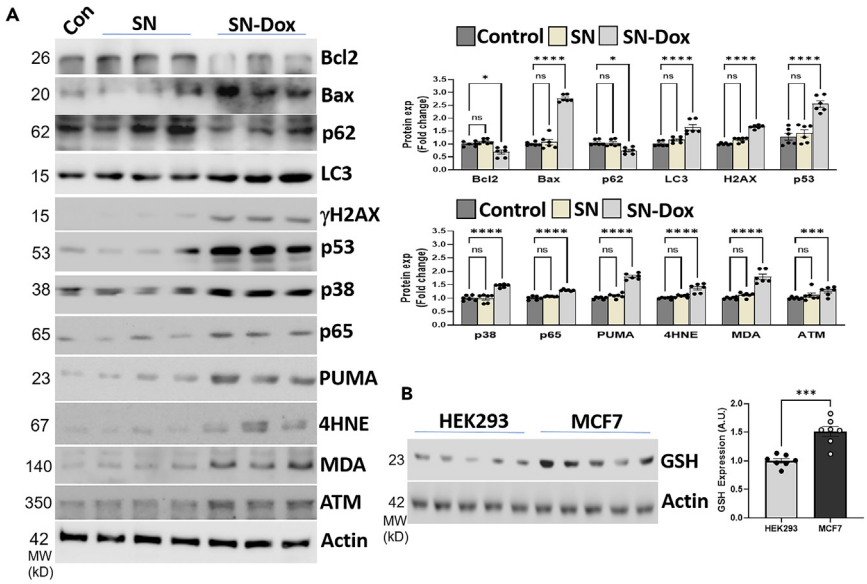

Figure 11. Expression of various proteins

(A) apoptotic proteins were measured in MCF7 cells treated with SN or SN-Dox and untreated control group and (B) GSH expression in embryonic kidney HEK293 cells and breast cancer cell MCF7. No significant changes were visible in control cells and with SN treatment whereas SN-Dox caused a significant change in the protein expressions. β-actin was used as a loading control for all the western blots. All results are reported as means + S.E. (n=6, *p<0.05, **p<0.01, ***p<0.001, ****p<0.0001 compared to control group).

down-regulating anti-apoptotic protein Bcl-2. Simultaneously, additional kinases including p38 and p65 facilitate ROS generation, which can lead to lipid peroxidation as indicated by increases in markers malondialdehyde (MDA) and 4-hydroxynonenal (4HNE). p53 is also known to modulate autophagic flux inside the cell to help aid in removal of damaged proteins and organelles as indicated by changes in protein levels of autophagy markers LC3 and p62 following p53 induction (Figure 12).[58] Importantly, SN-Dox, but not SN alone, altered expression of proteins in these cascades in MCF7 cells (Figure 11A). Finally, as a control, we confirmed elevated levels of GSH in MCF7 cells as compared to non-malignant cells (Figure 11B). Together our *in vitro* data are consistent with the ability of elevated GSH in cancer cells to facilitate cleavage of disulfide bonds in the SN assembly allowing for more efficient Dox release into cancer cells. Once released, as with the unencapsulated drug, SN-Dox can trigger cell death via several mechanisms. This represents the first evidence of functionalization of a redox-responsive disulfide-containing short peptide capable of facilitating cell type-selective delivery of a cancer chemotherapeutic.

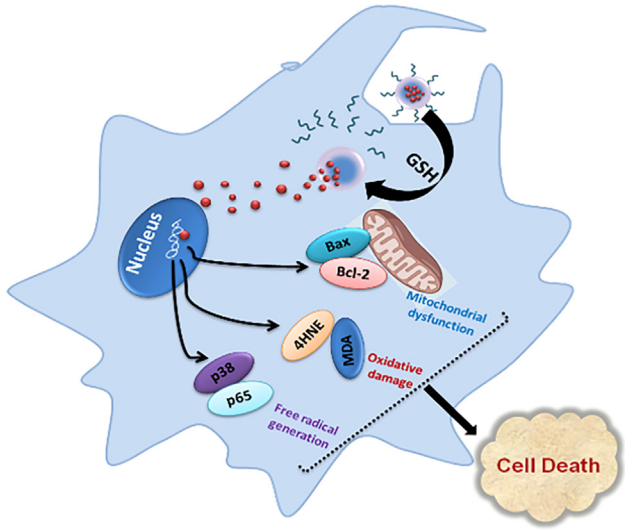

Figure 12. The schematic representation diagram of the cellular apoptotic pathway activated by GSH leading to breakdown of disulfide bond in cancer cell releasing Dox encapsulated in synthesized compound

In conclusion, we have described the self-assembly of a cysteine-cored diphenylalanine-appended tetrapeptide (SN) into hollow spheres, which can be successfully employed as an efficient vehicle for delivery of chemotherapeutic drugs such as Dox into cancer cells. These SN-based hollow spheres effectively encapsulated anticancer drug Dox and exhibited redox-responsive release of the desired drug owing to the reductive cleavage of the disulfide functionality in the presence of tumor-relevant GSH levels. The internalization of the Dox-entrapped hollow spheres into cancer cells and their consequent GSH-triggered redox-responsive drug release led to rapid death of cancer cells while sparing non-malignant cell types. Furthermore, the visible fluorescence of the self-assembled SN allows the real-time monitoring of the encapsulated drug's release directly into cells. Moreover, the slow release of the desired drug to the targeted site may help minimize off-target effects. While redox-sensitive release of encapsulated Dox has been previously achieved,[40] our SN-based drug delivery platform can be considered as a superior approach based on the following aspects. First, the FF (Phe-Phe) dipeptide backbone self-assembles into stimuli-responsive hollow spheres with nanometric dimensions and intrinsic fluorescence properties allowing for clinical utility as not only a drug delivery vehicle but also optical imaging probe that could allow monitoring of real-time drug release. Second, we confirm that encapsulation of Dox within the SN-based assembly not only allows for drug delivery into cancer cells but fails to impede the cancer-killing actions of Dox, a requirement for *in vivo* applications. Thus, this disulfide-functionalized peptide (SN)-based hollow spheres represent a superior platform for the development of effectual imaging probe or site-specific drug delivery vehicle for various bio-medical applications.

Limitations of the study

While SN-Dox-driven cytotoxicity was lower in non-malignant cells as compared to cancer cells, based on our drug release studies there is likely to be some leak of encapsulated drug even in the absence of GSH. This represents a notable limitation to the employment of SN-based drug delivery vehicles *in vivo*. Selectivity of drug release might be enhanced via the addition of surface modification or functional groups to increase chemotherapeutic drug affinity thereby decreasing leak of drug from intact SN spheres. In addition, functional groups might also be added to direct the entry of SN-based nanostructures specifically into cancerous cells while sparing surrounding tissue. We should also note that, to date, our investigations into the stability, site specificity, and efficacy of SN-Dox as an anticancer agent have been limited to *in vitro* experiments and await confirmation of pharmacokinetic and pharmacodynamic properties *in vivo*.

STAR★METHODS

Detailed methods are provided in the online version of this paper and include the following:

- KEY RESOURCES TABLE
- RESOURCE AVAILABILITY
  - Lead contact
  - Materials availability
  - Data and code availability
- EXPERIMENTAL MODEL AND STUDY PARTICIPANT DETAILS
  - Cell culture
- METHOD DETAILS
  - Synthesis of SN
  - Self-assembly of SN
  - High resolution scanning electron microscopy (HR-SEM)
  - Transmission electron microscopy (TEM)
  - Computer aided design (CAD) of SN peptide hollow structure
  - Fourier transform infrared spectroscopy (FT-IR)
  - UV-Vis spectroscopy
  - Fluorescence spectroscopy
  - Dynamic light scattering (DLS) analysis
  - Drug loading and drug release of SN-Based self-assembled superstructures
  - Drug-encapsulation efficiency (EE) and loading capacity (LC) calculation
  - In vitro drug release studies
  - MTT assay
  - Fluorometric analysis
  - Immunofluorescence study
  - ROS generation study
  - Measurement of mitochondrial membrane potential
  - Apoptosis assay
  - DNA fragmentation assay
  - Immunoblotting
- QUANTIFICATION AND STATISTICAL ANALYSIS

SUPPLEMENTAL INFORMATION

Supplemental information can be found online at https://doi.org/10.1016/j.isci.2024.109523.

ACKNOWLEDGMENTS

P.D. acknowledges the Board of Research in Nuclear Sciences (BRNS), India, for research funding (grant no. 58/14/14/2021-BRNS/37219) and the support of the Interdisciplinary Institute of Indian System of Medicine (IIISM) for providing NMR and ESI Mass Spectrometry Facility, Nano Research Centre (NRC), and the Department of Biotechnology (DBT) of the SRM Institute of Science and Technology for several characterization studies. B.M. acknowledges the fund from the Indian Council of Medical Research (grant no. ICMR, 5/4/1-22/CVD/2022 NCD-I).

AUTHOR CONTRIBUTIONS

Conceptualization and methodology, P.D. and B.M.; software, D.K.; acquisition of data, S.N., K.D., S.S., S.B., and D.K.; analysis, investigation, and interpretation of data, S.N., K.D., S.S., A.S., D.K., B.M., and P.D.; writing – original draft and writing – review and editing, S.N., S.S., K.D., A.S., D.K., B.M., and P.D.; visualization, S.N., K.D., S.S., A.S., D.K., B.M., and P.D.; supervision, P.D. and B.M.; S.N., K.D., and S.S., contributed equally.

DECLARATION OF INTERESTS

The authors declare no competing interests.

Received: November 29, 2023
Revised: February 13, 2024
Accepted: March 14, 2024
Published: March 16, 2024

REFERENCES

1. Liu, D., Yang, F., Xiong, F., and Gu, N. (2016). The smart drug delivery system and its clinical potential. Theranostics *6*, 1306–1323. https://doi.org/10.7150/thno.14858.
2. Wang, Y.-F., Liu, L., Xue, X., and Liang, X.-J. (2017). Nanoparticle-based drug delivery systems: What can they really do in vivo? F1000Res. *6*, 681. https://doi.org/10.12688/f1000research.9690.1.
3. Li, Z., Tan, S., Li, S., Shen, Q., and Wang, K. (2017). Cancer drug delivery in the nano era: An overview and perspectives. Oncol. Rep. *38*, 611–624. https://doi.org/10.3892/or.2017.5718.
4. Pramanik, S.K., and Das, A. (2021). Fluorescent probes for imaging bioactive species in subcellular organelles. Chem. Commun. *57*, 12058–12073. https://doi.org/10.1039/D1CC04273D.
5. Pramanik, S.K., Sreedharan, S., Tiwari, R., Dutta, S., Kandoth, N., Barman, S., Aderinto, S.O., Chattopadhyay, S., Das, A., and Thomas, J.A. (2022). Nanoparticles for super-resolution microscopy: intracellular delivery and molecular targeting. Chem. Soc. Rev. *51*, 9882–9916. https://doi.org/10.1039/D1CS00605C.
6. Ramu, V., Ali, F., Taye, N., Garai, B., Alam, A., Chattopadhyay, S., and Das, A. (2015). New imaging reagents for lipid dense regions in live cells and the nucleus in fixed MCF-7 cells. J. Mater. Chem. B *3*, 7177–7185. https://doi.org/10.1039/C5TB01309G.
7. Sharma, A., and Sharma, U.S. (1997). Liposomes in drug delivery: Progress and limitations. Int. J. Pharm. X. *154*, 123–140. https://doi.org/10.1016/S0378-5173(97)00135-X.
8. Alavi, M., Karimi, N., and Safaei, M. (2017). Application of Various Types of Liposomes in Drug Delivery Systems. Adv. Pharmaceut. Bull. *7*, 3–9. https://doi.org/10.15171/apb.2017.002.
9. Moreno Raja, M., Lim, P.Q., Wong, Y.S., Xiong, G.M., Zhang, Y., Venkatraman, S., and Huang, Y. (2019). Polymeric Nanomaterials (Elsevier Inc.). https://doi.org/10.1016/b978-0-12-814033-8.00018-7.
10. Ahmad, Z., Shah, A., Siddiq, M., and Kraatz, H.-B. (2014). Polymeric micelles as drug delivery vehicles. RSC Adv. *4*, 17028–17038. https://doi.org/10.1039/C3RA47370H.
11. Chauhan, A.S. (2018). Dendrimers for Drug Delivery. Molecules *23*, 938. https://doi.org/10.3390/molecules23040938.
12. Sreedharan, S., Tiwari, R., Tyde, D., Aderinto, S.O., Pramanik, S.K., Das, A., and Thomas, J.A. (2021). Nanocarriers used as probes for super-resolution microscopy. Mater. Chem. Front. *5*, 1268–1282. https://doi.org/10.1039/D0QM00684J.
13. Sivagnanam, S., Das, K., Pan, I., Barik, A., Stewart, A., Maity, B., and Das, P. (2023). Functionalized Fluorescent Nanostructures Generated from Self-Assembly of a Cationic Tripeptide Direct Cell-Selective Chemotherapeutic Drug Delivery. ACS Appl. Bio Mater. *6*, 836–847. https://doi.org/10.1021/acsabm.2c00996.
14. Panda, J.J., Kaul, A., Kumar, S., Alam, S., Mishra, A.K., Kundu, G.C., and Chauhan, V.S. (2013). Modified dipeptide-based nanoparticles: Vehicles for targeted tumor drug delivery. Nanomedicine *8*, 1927–1942. https://doi.org/10.2217/nnm.12.201.
15. Wei, G., Wang, Y., Huang, X., Hou, H., and Zhou, S. (2018). Peptide-Based Nanocarriers for Cancer Therapy. Small Methods *2*, 1–16. https://doi.org/10.1002/smtd.201700358.
16. Mura, S., Nicolas, J., and Couvreur, P. (2013). Stimuli-responsive nanocarriers for drug delivery. Nat. Mater. *12*, 991–1003. https://doi.org/10.1038/nmat3776.
17. Pramanik, S.K., Pal, U., Choudhary, P., Singh, H., Reiter, R.J., Ethirajan, A., Swarnakar, S., and Das, A. (2019). Stimuli-Responsive Nanocapsules for the Spatiotemporal Release of Melatonin: Protection against Gastric Inflammation. ACS Appl. Bio Mater. *2*, 5218–5226. https://doi.org/10.1021/acsabm.9b00236.
18. Linsley, C.S., and Wu, B.M. (2017). Recent advances in light-responsive on-demand drug-delivery systems. Ther. Deliv. *8*, 89–107. https://doi.org/10.4155/tde-2016-0060.
19. Yeingst, T.J., Arrizabalaga, J.H., and Hayes, D.J. (2022). Ultrasound-Induced Drug Release from Stimuli-Responsive Hydrogels. Gels *8*, 554. https://doi.org/10.3390/gels8090554.
20. Zha, L., Banik, B., and Alexis, F. (2011). Stimulus responsive nanogels for drug delivery. Soft Matter *7*, 5908–5916. https://doi.org/10.1039/c0sm01307b.
21. Shahriari, M., Zahiri, M., Abnous, K., Taghdisi, S.M., Ramezani, M., and Alibolandi, M. (2019). Enzyme responsive drug delivery systems in cancer treatment. J. Contr. Release *308*, 172–189. https://doi.org/10.1016/j.jconrel.2019.07.004.
22. Bikram, M., and West, J.L. (2008). Thermo-responsive systems for controlled drug delivery. Expet Opin. Drug Deliv. *5*, 1077–1091. https://doi.org/10.1517/17425247.5.10.1077.
23. Zhu, Y.J., and Chen, F. (2015). pH-Responsive Drug-Delivery Systems. Chem. Asian J. *10*, 284–305. https://doi.org/10.1002/asia.201402715.
24. Cheng, R., Feng, F., Meng, F., Deng, C., Feijen, J., and Zhong, Z. (2011). Glutathione-responsive nano-vehicles as a promising platform for targeted intracellular drug and gene delivery. J. Contr. Release *152*, 2–12.

https://doi.org/10.1016/j.jconrel.2011.01.030.
25. Rahim, M.A., Jan, N., Khan, S., Shah, H., Madni, A., Khan, A., Jabar, A., Khan, S., Elhissi, A., Hussain, Z., et al. (2021). Recent Advancements in Stimuli Responsive Drug Delivery Platforms for Active and Passive Cancer Targeting. Cancers *13*, 670. https://doi.org/10.3390/cancers13040670.
26. Townsend, D.M., Tew, K.D., and Tapiero, H. (2003). The importance of glutathione in human disease. Biomed. Pharmacother. *57*, 145–155. https://doi.org/10.1016/S0753-3322(03)00043-X.
27. Pal, S., Ramu, V., Taye, N., Mogare, D.G., Yeware, A.M., Sarkar, D., Reddy, D.S., Chattopadhyay, S., and Das, A. (2016). GSH Induced Controlled Release of Levofloxacin from a Purpose-Built Prodrug: Luminescence Response for Probing the Drug Release in Escherichia coli and Staphylococcus aureus. Bioconjugate Chem. *27*, 2062–2070. https://doi.org/10.1021/acs.bioconjchem.6b00324.
28. Li, S., Chang, R., Zhao, L., Xing, R., van Hest, J.C.M., and Yan, X. (2023). Two-photon nanoprobes based on bioorganic nanoarchitectonics with a photo-oxidation enhanced emission mechanism. Nat. Commun. *14*, 5227. https://doi.org/10.1038/s41467-023-40897-4.
29. Ballatori, N., Krance, S.M., Notenboom, S., Shi, S., Tieu, K., and Hammond, C.L. (2009). Glutathione dysregulation and the etiology and progression of human diseases. bchm *390*, 191–214. https://doi.org/10.1515/BC.2009.033.
30. Mollazadeh, S., Mackiewicz, M., and Yazdimamaghani, M. (2021). Recent advances in the redox-responsive drug delivery nanoplatforms: A chemical structure and physical property perspective. Mater. Sci. Eng. C *118*, 111536. https://doi.org/10.1016/j.msec.2020.111536.
31. Bansal, A., and Simon, M.C. (2018). Glutathione metabolism in cancer progression and treatment resistance. J. Cell Biol. *217*, 2291–2298. https://doi.org/10.1083/jcb.201804161.
32. Kim, J.E., Cha, E., and Ahn, C. (2010). Reduction-Sensitive Self-Aggregates as a Novel Delivery System. Macromol. Chem. Phys. *211*, 956–961. https://doi.org/10.1002/macp.200900671.
33. Rissanou, A.N., Georgilis, E., Kasotakis, E., Mitraki, A., and Harmandaris, V. (2013). Effect of Solvent on the Self-Assembly of Dialanine and Diphenylalanine Peptides. J. Phys. Chem. B *117*, 3962–3975. https://doi.org/10.1021/jp311795b.
34. Maity, S., Jana, P., Maity, S.K., and Haldar, D. (2011). Fabrication of Hollow Self-Assembled Peptide Microvesicles and Transition from Sphere-to-Rod Structure. Langmuir *27*, 3835–3841. https://doi.org/10.1021/la104461m.
35. Lv, K., Zhang, L., and Liu, M. (2014). Self-Assembly of Triangular Amphiphiles into Diverse Nano/Microstructures and Release Behavior of the Hollow Sphere. Langmuir *30*, 9295–9302. https://doi.org/10.1021/la502335p.
36. Zhou, P., Xing, R., Li, Q., Li, J., Yuan, C., and Yan, X. (2023). Steering phase-separated droplets to control fibrillar network evolution of supramolecular peptide hydrogels. Matter *6*, 1945–1963. https://doi.org/10.1016/j.matt.2023.03.029.
37. Yuan, C., Li, Q., Xing, R., Li, J., and Yan, X. (2023). Peptide self-assembly through liquid-liquid phase separation. Chem *9*, 2425–2445. https://doi.org/10.1016/j.chempr.2023.05.009.
38. Xing, R., Yuan, C., Fan, W., Ren, X., and Yan, X. (2023). Biomolecular glass with amino acid and peptide nanoarchitectonics. Sci. Adv. *9*, eadd8105–12. https://doi.org/10.1126/sciadv.add8105.
39. Yuan, C., Levin, A., Chen, W., Xing, R., Zou, Q., Herling, T.W., Challa, P.K., Knowles, T.P.J., and Yan, X. (2019). Nucleation and Growth of Amino Acid and Peptide Supramolecular Polymers through Liquid–Liquid Phase Separation. Angew. Chem., Int. Ed. Engl. *58*, 18116–18123. https://doi.org/10.1002/anie.201911782.
40. Dhawan, S., Ghosh, S., Ravinder, R., Bais, S.S., Basak, S., Krishnan, N.M.A., Agarwal, M., Banerjee, M., and Haridas, V. (2019). Redox Sensitive Self-Assembling Dipeptide for Sustained Intracellular Drug Delivery. Bioconjugate Chem. *30*, 2458–2468. https://doi.org/10.1021/acs.bioconjchem.9b00532.
41. Zhu, P., Yan, X., Su, Y., Yang, Y., and Li, J. (2010). Solvent-Induced Structural Transition of Self-Assembled Dipeptide: From Organogels to Microcrystals. Chem. Eur J. *16*, 3176–3183. https://doi.org/10.1002/chem.200902139.
42. Ozvoldik, K., Stockner, T., and Krieger, E. (2023). YASARA Model–Interactive Molecular Modeling from Two Dimensions to Virtual Realities. J. Chem. Inf. Model. *63*, 6177–6182. https://doi.org/10.1021/acs.jcim.3c01136.
43. Feeney, K.A., Wellner, N., Gilbert, S.M., Halford, N.G., Tatham, A.S., Shewry, P.R., and Belton, P.S. (2003). Molecular structures and interactions of repetitive peptides based on wheat glutenin subunits depend on chain length. Biopolymers *72*, 123–131. https://doi.org/10.1002/bip.10298.
44. Kong, J., and Yu, S. (2007). Fourier transform infrared spectroscopic analysis of protein secondary structures. Acta Biochim. Biophys. Sin. *39*, 549–559. https://doi.org/10.1111/j.1745-7270.2007.00320.x.
45. Mauerer, A., and Lee, G. (2006). Changes in the amide I FT-IR bands of poly-l-lysine on spray-drying from α-helix, β-sheet or random coil conformations. Eur. J. Pharm. Biopharm. *62*, 131–142. https://doi.org/10.1016/j.ejpb.2005.08.005.
46. Greenfield, N.J. (2006). Using circular dichroism spectra to estimate protein secondary structure. Nat. Protoc. *1*, 2876–2890. https://doi.org/10.1038/nprot.2006.202.
47. Das, P., Ghosh, A., Bhatt, H., and Das, A. (2012). A highly selective and dual responsive test paper sensor of Hg 2+/Cr 3+ for naked eye detection in neutral water. RSC Adv. *2*, 3714–3721. https://doi.org/10.1039/c2ra00788f.
48. Na, N., Mu, X., Liu, Q., Wen, J., Wang, F., and Ouyang, J. (2013). Self-assembly of diphenylalanine peptides into microtubes with "turn on" fluorescence using an aggregation-induced emission molecule. Chem. Commun. *49*, 10076–10078. https://doi.org/10.1039/c3cc45320k.
49. Fu, D., Liu, D., Zhang, L., and Sun, L. (2020). Self-assembled fluorescent tripeptide nanoparticles for bioimaging and drug delivery applications. Chin. Chem. Lett. *31*, 3195–3199. https://doi.org/10.1016/j.cclet.2020.07.011.
50. Yuan, W.Z., Lu, P., Chen, S., Lam, J.W.Y., Wang, Z., Liu, Y., Kwok, H.S., Ma, Y., and Tang, B.Z. (2010). Changing the Behavior of Chromophores from Aggregation-Caused Quenching to Aggregation-Induced Emission: Development of Highly Efficient Light Emitters in the Solid State. Adv. Mater. *22*, 2159–2163. https://doi.org/10.1002/adma.200904056.
51. Luo, J., Xie, Z., Lam, J.W., Cheng, L., Chen, H., Qiu, C., Kwok, H.S., Zhan, X., Liu, Y., Zhu, D., and Tang, B.Z. (2001). Aggregation-induced emission of 1-methyl-1,2,3,4,5-pentaphenylsilole. Chem. Commun. *18*, 1740–1741. https://doi.org/10.1039/b105159h.
52. Liu, K., Zhang, R., Li, Y., Jiao, T., Ding, D., and Yan, X. (2017). Tunable Aggregation-Induced Emission of Tetraphenylethylene via Short Peptide-Directed Self-Assembly. Adv. Mater. Interfac. *4*. https://doi.org/10.1002/admi.201600183.
53. Mainz, E.R., Dobes, N.C., and Allbritton, N.L. (2015). Pronase E-Based Generation of Fluorescent Peptide Fragments: Tracking Intracellular Peptide Fate in Single Cells. Anal. Chem. *87*, 7987–7995. https://doi.org/10.1021/acs.analchem.5b01929.
54. Lee, M.H., Yang, Z., Lim, C.W., Lee, Y.H., Dongbang, S., Kang, C., and Kim, J.S. (2013). Disulfide-Cleavage-Triggered Chemosensors and Their Biological Applications. Chem. Rev. *113*, 5071–5109. https://doi.org/10.1021/cr300358b.
55. Wang, T., Ng, D.Y.W., Wu, Y., Thomas, J., TamTran, T., and Weil, T. (2014). Bis-sulfide bioconjugates for glutathione triggered tumor responsive drug release. Chem. Commun. *50*, 1116–1118. https://doi.org/10.1039/C3CC47003B.
56. Wang, J., Sun, X., Mao, W., Sun, W., Tang, J., Sui, M., Shen, Y., and Gu, Z. (2013). Tumor Redox Heterogeneity-Responsive Prodrug Nanocapsules for Cancer Chemotherapy. Adv. Mater. *25*, 3670–3676. https://doi.org/10.1002/adma.201300929.
57. Jia, L., Cui, D., Bignon, J., Di Cicco, A., Wdzieczak-Bakala, J., Liu, J., and Li, M.-H. (2014). Reduction-Responsive Cholesterol-Based Block Copolymer Vesicles for Drug Delivery. Biomacromolecules *15*, 2206–2217. https://doi.org/10.1021/bm5003569.
58. Lee, M.H., Sessler, J.L., and Kim, J.S. (2015). Disulfide-Based Multifunctional Conjugates for Targeted Theranostic Drug Delivery. Acc. Chem. Res. *48*, 2935–2946. https://doi.org/10.1021/acs.accounts.5b00406.
59. Ozvoldik, K., Stockner, T., Rammner, B., and Krieger, E. (2021). Assembly of Biomolecular Gigastructures and Visualization with the Vulkan Graphics API. J. Chem. Inf. Model. *61*, 5293–5303. https://doi.org/10.1021/acs.jcim.1c00743.
60. Krieger, E., and Vriend, G. (2014). YASARA View—molecular graphics for all devices—from smartphones to workstations. Bioinformatics *30*, 2981–2982. https://doi.org/10.1093/bioinformatics/btu426.
61. Raj, R., Agarwal, N., Raghavan, S., Chakraborti, T., Poluri, K.M., Pande, G., and Kumar, D. (2021). Epigallocatechin Gallate with Potent Anti- Helicobacter pylori Activity Binds Efficiently to Its Histone-like DNA Binding Protein. ACS Omega *6*, 3548–3570. https://doi.org/10.1021/acsomega.0c04763.
62. Zhang, Z., and Feng, S.-S. (2006). The drug encapsulation efficiency, in vitro drug release, cellular uptake and cytotoxicity of paclitaxel-loaded poly(lactide)–tocopheryl polyethylene glycol succinate nanoparticles. Biomaterials *27*, 4025–4033. https://doi.org/10.1016/j.biomaterials.2006.03.006.

63. Basak, M., Mahata, T., Chakraborti, S., Kumar, P., Bhattacharya, B., Bandyopadhyay, S.K., Das, M., Stewart, A., Saha, S., and Maity, B. (2020). Malabaricone C attenuates nonsteroidal anti-inflammatory drug-induced gastric ulceration by decreasing oxidative/nitrative stress and inflammation and promoting angiogenic autohealing. Antioxidants Redox Signal. *32*, 766–784. https://doi.org/10.1089/ars.2019.7781.

64. Rajput, A., De, A., Mondal, A., Das, K., Maity, B., and Husain, S.M. (2022). A biocatalytic approach towards the preparation of natural deoxyanthraquinones and their impact on cellular viability. New J. Chem. *46*, 3087–3090. https://doi.org/10.1039/D1NJ05513E.

65. Sivagnanam, S., Das, K., Basak, M., Mahata, T., Stewart, A., Maity, B., and Das, P. (2022). Self-assembled dipeptide based fluorescent nanoparticles as a platform for developing cellular imaging probes and targeted drug delivery chaperones. Nanoscale Adv. *4*, 1694–1706. https://doi.org/10.1039/D1NA00885D.

66. Sivagnanam, S., Das, K., Sivakadatcham, V., Mahata, T., Basak, M., Pan, I., Stewart, A., Maity, B., and Das, P. (2022). Generation of Self-Assembled Structures Composed of Amphipathic, Charged Tripeptides for Intracellular Delivery of Pro-Apoptotic Chemotherapeutics. Isr. J. Chem. *62*, e202200001. https://doi.org/10.1002/ijch.202200001.

67. Das, K., Basak, M., Mahata, T., Biswas, S., Mukherjee, S., Kumar, P., Moniruzzaman, M., Stewart, A., and Maity, B. (2023). Cardiac RGS7 and RGS11 drive TGFβ1-dependent liver damage following chemotherapy exposure. Faseb. J. *37*, e23064. https://doi.org/10.1096/fj.202300094R.

68. Basak, M., Sengar, A.S., Das, K., Mahata, T., Kumar, M., Kumar, D., Biswas, S., Sarkar, S., Kumar, P., Das, P., et al. (2023). A RGS7-CaMKII complex drives myocyte-intrinsic and myocyte-extrinsic mechanisms of chemotherapy-induced cardiotoxicity. Proc. Natl. Acad. Sci. USA *120*, e2213537120. https://doi.org/10.1073/pnas.2213537120.

STAR★METHODS

KEY RESOURCES TABLE

REAGENT or RESOURCE	SOURCE	IDENTIFIER
Chemicals, peptides, and recombinant proteins		
L-Phenylalanine	SRL	CAS: 63-91-2
L-Cystine	SRL	CAS: 56-89-3
N,N′- Dicyclohexylcarbodiimide (DCC)	SRL	CAS: 538-75-0
1-Hydroxy benzotriazole (HOBt)	SRL	CAS:2592-95-2
Boc anhydride	SRL	CAS:24424-99-5
Trimethylchlorosilane (TMSCl)	SRL	CAS:75-77-4
Triethyl amine	SRL	CAS:121-44-8
Potassium hydrogen sulfate	Finar	CAS: 7646-93-7
Hydrochloric Acid (HCl)	Finar	CAS: 7647-01-0
Sodium chloride	Finar	CAS: 7647-14-5
Sodium sulfate	Finar	CAS: 7757-82-6
Sodium hydroxide	Finar	CAS: 1310-73-2
Sodium carbonate	Finar	CAS: 497-19-8
1,1,1,3,3,3- hexafluoro-2propanol (HFP)	Sigma Aldrich	CAS: 920-66-1
Doxorubicin dye	Sigma Aldrich	CAS: 23214-92-8
2′,7′-Dichlorofluorescin diacetate (CM-H_2DCFDA)	Sigma Aldrich	CAS: 4091-99-0
Dimethyl sulfoxide (DMSO)	Sigma Aldrich	CAS: 67-68-5
2′,7′-Dichlorofluorescin diacetate (CM-H_2DCFDA)	Sigma Aldrich	CAS Number: 4091-99-0 CAS Number: 4091-99-0 CAS Number: 4091-99-0 CAS: 4091-99-0
Doxorubicin	Abcam	CAS: 25316-40-9
ECL substrate kit	Abcam	Cat# ab133406
Protease inhibitor cocktail	Abcam	Cat# ab201111
Phosphatase inhibitor cocktail	Abcam	Cat# ab201112
Dulbecco's Modified Eagle Medium (DMEM)	Thermo Fisher Scientific	Cat# 12100046
Trypsin EDTA 0.05%	Thermo Fisher Scientific	Cat# 25300062
10X RIPA	Himedia	Cat# TCL131
Fetal bovine serum (FBS)	Himedia	Cat# RM1112
Phosphate Buffer Saline (PBS)	Himedia	Cat# TL1101
Antibodies		
Bcl2 antibody	Abcam	Cat# ab59348
Bax antibody	Cell Signaling Technology	Cat# 2772S
p62 antibody	Abcam	Cat# ab91526
p65 antibody	Cell Signaling Technology	Cat# 8242S
4HNE antibody	Abcam	Cat# ab46545
β-Actin antibody	Abcam	Cat# ab8227
LC3 antibody	Abcam	Cat# ab48394
p53 antibody	Cell Signaling Technology	Cat# 9282S
p38 antibody	Cell Signaling Technology	Cat# 9212S
H2AX antibody	Abcam	Cat#ab11174

(*Continued on next page*)

Continued

REAGENT or RESOURCE	SOURCE	IDENTIFIER
PUMA antibody	Cell Signaling Technology	Cat# 4976S
MDA antibody	Abcam	Cat#ab27642
ATM antibody	Cell Signaling Technology	Cat# 2873S
GSH antibody	Invitrogen	Cat# MA1-7620
Experimental models: Cell lines		
HEK293 cells	National Centre for Cell Science (NCCS) in Pune, India	N/A
MCF7 cells	National Centre for Cell Science (NCCS) in Pune, India	N/A
MDA-MB-231 cells	National Centre for Cell Science (NCCS) in Pune, India	N/A
AC16 cells	Sigma Aldrich	Cat#SCC109
Software and algorithms		
GraphPad Prism 9	GraphPad	N/A
ChemDraw Ultra 12.0	PerkinElmer	https://www.perkinelmer.com/category/chemdraw.
MestReNova	Mestrelab Research chemistry software solutions.	https://mestrelab.com/
OriginPro 8.5	OriginLab	https://www.originlab.com/
YASARA	YASARA Biosciences	http://www.yasara.org/
ImageJ	NIH	https://imagej.nih.gov/ij/index.html

RESOURCE AVAILABILITY

Lead contact

Further information and requests for material should be directed to and will be fulfilled by the lead contact, Priyadip Das (priyadipcsmcri@gmail.com, priyadip@srmist.edu.in).

Materials availability

This study did not generate new unique reagents.

Data and code availability

- Data: All data reported in this paper will be shared by the lead contact upon request.
- Code: This paper does not report the original code.
- Any additional information required to reanalyze the data reported in this paper is available from the lead contact upon request.

EXPERIMENTAL MODEL AND STUDY PARTICIPANT DETAILS

Cell culture

The human embryonic kidney (HEK293) and breast cancer (MCF7 and MDAMB231) cell lines were supplied by the National Center for Cell Science (NCCS) in Pune, India. The human cardiac myocyte cell line (AC16) was procured from Merck, Millipore, USA. The cells at passages 3–5 were cultured in DMEM media with 10% FBS, 100 U/mL penicillin, and 100 μg/mL streptomycin at a standard condition of 37°C temperature within a 5% CO_2 incubation environment. All the cells were authenticated by observing their morphology under the microscope carefully and cultured in a strict mycoplasma-free conditions.[63]

METHOD DETAILS

All chemicals and solvents are commercially available and were used as received. L-Phenylalanine, L-Cystine, N,N′- Dicyclohexylcarbodiimide (DCC),1-Hydroxy benzotriazole (HOBt), Boc anhydride, Trimethylchlorosilane (TMSCl), Triethyl amine were purchased from Sisco Research Laboratories Pvt. Ltd. (SRL, India). Potassium hydrogen sulfate, HCl, Sodium chloride, Sodium sulfate, Sodium hydroxide, Sodium carbonate was purchased from Finar Chemicals Pvt. Ltd (India). 1,1,1,3,3,3- hexafluoro-2propanol (HFP), and Doxorubicin dye were purchased from Sigma Aldrich. 2′,7′-Dichlorofluorescin diacetate (CM-H_2DCFDA) and Dimethyl sulfoxide (DMSO) were purchased from Sigma Aldrich (St. Louis, MO, USA). Doxorubicin, ECL substrate kit, Protease inhibitor cocktail, and Phosphatase inhibitor cocktail were obtained from Abcam (Cambridge, UK). Dulbecco's Modified Eagle Medium (DMEM) and Trypsin EDTA 0.05% were procured from Thermo Fisher Scientific

(Waltham, MA, USA). 10X RIPA, Fetal bovine serum (FBS), and Phosphate Buffer Saline (PBS) were purchased from Himedia (Mumbai, India). Other standard laboratory chemicals and reagents were purchased from Sisco Research Laboratories (SRL) Pvt. Ltd, India.

Synthesis of SN

Experimental Section

Peptide synthesis. Peptides were synthesized by conventional solution-phase methods. Peptide coupling was mediated by dicyclohexyl-carbodiimide/1-hydroxybenzotriazole (DCC/HOBt). The products were purified by column chromatography using silica gel (100–200 mesh) as the stationary phase and an n-hexane–ethyl acetate mixture as an eluent. The final compounds were fully characterized by Bruker 500 MHz ^{1}H-NMR spectroscopy, and mass spectroscopy (Shimadzu, Japan, LCMS-2020 Spectrometer).

Synthesis of BOC-NH-Phe-OH (S1). A solution of L-phenylalanine (3 g, 18.16 mmol) in a mixture of dioxane (45 mL), water (25 mL), and 1 M NaOH (18 mL) was stirred and cooled in an ice water bath. 4.35 g of di-tert-butyl dicarbonate was added and stirred continuously at room temperature (RT) for 6 hrs. Then, the solution was concentrated using a rotary evaporator to about 10–15 mL, cooled in an ice-water bath, covered with a layer of ethyl acetate (about 50 mL), and acidified with a dilute solution of $KHSO_4$ to pH 2–3 (determined by congo red). The aqueous phase was extracted with ethyl acetate, and this operation was performed repeatedly. The ethyl acetate extracts were pooled, washed with water, dried over anhydrous Na_2SO_4, and evaporated under a vacuum. The pure material was obtained as a waxy solid. Yield: 4.54 g (17.11 mmol, 94.25%) (Scheme S1).

Synthesis of NH_2-Phe-OMe hydrochloride (S2). L-Phenylalanine 3g (18.16 mmol) was taken in a round bottom flask and dissolved in 60 mL MeOH. Then, 4.61 mL (36.32 mmol) of Trimethyl chlorosilane (TMSCl) was added to the resulting solution slowly in a drop wise manner and stirred for 8 hrs at room temperature. After the completion of reaction (as monitored by TLC), the excess solvent was evaporated on a rotary evaporator to get the solid desired product, L-Phenylalanine methyl ester hydrochloride. Yield: 3.76 g (17.43 mmol, 96.02%) (Scheme S1).

Synthesis of BOC-Phe-Phe-OMe (S3). 4.15 g (15.64 mmol) of Boc-Phe-OH(S1) were dissolved in 40 mL dry DCM in an ice-water bath. NH_2-Phe-OMe.HCl(S2) 4.05 g (18.77mmol) and Et_3N 2 ml were then added to the reaction mixture, followed immediately by the addition of 3.87 g (18.77 mmol) dicyclohexylcarbodiimide (DCC) and 2.53 g (18.77 mmol) of HOBt. The reaction mixture was allowed to warm up to RT and stirred for 48 hrs. DCM was evaporated, and the residue was dissolved in ethyl acetate (45 mL). The dicyclohexylurea (DCU) was filtered off. The organic layer was washed with 2M HCl (3 X 50 mL), brine (2 X 50 mL) followed by 1 M sodium carbonate (3 X 50 mL) and brine (2 X 50 mL), and finally dried over anhydrous sodium sulfate. It was then evaporated under a vacuum to yield Boc-Phe-Phe-OMe as a white solid. The product was purified by silica gel (100–200 mesh) using n-hexane–ethyl acetate (3:1) as eluent. Yield: 5.40 g (12.66 mmol, 80.96%) (Scheme S1).

Synthesis of BOC-NH-Phe-Phe-OH (S4). To 6.06 g (14.21 mmol) of Boc-Phe-Phe-OMe(S3), 40 mL MeOH and 2M 23 mL NaOH were added and the progress of saponification was monitored by thin layer chromatography (TLC). The reaction mixture was stirred. After 10 hrs, the methanol was removed under vacuum; the remaining residue was dissolved in 50 mL of water and washed with diethyl ether (2 X 50 mL). Then, the pH of the aqueous layer was adjusted to 2 using 1M HCl and extracted with ethyl acetate (3 X 50 mL). The extracts were pooled, dried over anhydrous sodium sulfate, and evaporated under a vacuum to obtain the compound as a waxy solid. Yield: 5.74 g (13.91 mmol, 97.95%). (Scheme S1).

Synthesis of Cystine-OMe (S5). 2g (8.32 mmol) of L-Cystine was dissolved in 40 ml of MeOH and cooled in an ice bath. Then, 4.5 ml of TMSCl was added dropwise and stirred for 8hrs. The excess solvent was evaporated using a rotary vacuum. The dried crystalline solid product obtained was L-Cystine methyl ester hydrochloride. Yield 2.38 g (7.81 mmol, 94.07%) (Scheme S2).

Synthesis of BOC-Phe-Phe-Cys-Phe-Phe-BOC (SN). 763.66 mg (1.85 mmol) of Boc-Phe-Phe-OH (S4) were dissolved in 40 mL dry DCM in an ice water bath. Cys-OMe.HCl (S5) 282 mg (0.92 mmol) and Et_3N 2 ml were then added to the reaction mixture, followed immediately by the addition of 839.76 mg (4.07 mmol) dicyclohexylcarbodiimide (DCC) and 549.94 mg (4.07 mmol) of HOBt. The reaction mixture was allowed to warm up to RT and was stirred for 48 hrs. DCM was evaporated, and the residue was dissolved in ethyl acetate (45 mL). The dicyclohexylurea (DCU) was filtered off. The organic layer was washed with 2M HCl (3 X 50 mL), brine (2 X 50 mL), 1 M sodium carbonate (3 X 50 mL), and brine (2 X 50 mL), and finally dried over anhydrous sodium sulfate. It was then evaporated using a vacuum to yield Boc-Phe-Phe-Cys-Phe-Phe-BOC as a white solid. Then, it was purified by column chromatography. Yield 832 mg (0.79 mmol, 85.53%). Then, it was characterized by ^{1}H-NMR and mass spectrometer. (^{1}H NMR, $CDCl_3$, 500 MHz, δppm): 7.4 (m, 2H, Ar-Phe), 7.26-7.13 (m, 12H, Ar-Phe), 7.11-7.07 (m, 4H, Ar-Phe), 6.95-6.93 (m, 2H, Ar-Phe), 4.89-4.77 (m, 4H, CαH of Phe), 4.42 (m, 2H, CαH of Cys), 3.70 (s, 6H, -OMe), 3.07-2.88 (m, 12H, CβH of Phe, CβH of Cys), 1.35 (s, 18H, Boc). ^{13}C NMR (126 MHz, $CDCl_3$, δ_{ppm}): 171.74, 171.02, 170.20, 156.86, 136.72, 136.33, 129.44, 129.36, 128.57, 128.52, 126.87, 80.09, 54.22, 52.71, 52.27, 49.19, 39.94, 38.29, 38.15, 33.94, 29.70, 28.30, 25.62, 24.95. ESI MS (m/z): $[M+Na]^+$ = 1079.4234 (calculated); 1079.4500 (observed).

Self-assembly of SN

A fresh stock solution of the peptide was prepared by dissolving the lyophilized forms of the SN in HFP to a concentration of 100 mg mL^{-1}. Then, we blended this peptide solution in several proportions and diluted them with water to get the desired peptide concentrations for self-assembly. The polar solvent allowed the molecules to self-assemble.

High resolution scanning electron microscopy (HR-SEM)

A 20 μL drop of a self-assembled solution of SN was placed on a clean glass coverslip and allowed to dry at RT. SEM analysis was performed using a High-resolution scanning electron microscope (HR-SEM, Thermo scientific Apreo S) operating at 20 kV.

Transmission electron microscopy (TEM)

A 10 μL drop of a self-assembled solution of SN in 100% water was placed on a 200-mesh copper grid and covered by carbon-stabilized Formvars® film. After 1 min, excess fluid was removed from the grid. The samples were analysed using a transmission electron microscope, JEOL-JEM-2100 Plus (High-resolution scintillator) operating at 200 kV.

Computer aided design (CAD) of SN peptide hollow structure

The molecular model for self-assembled hollow structure of SN peptide containing drug was generated making composite use of commercial software CHEMDRAW (Perkin Elmer, v19.0.0.22) in combination with molecular docking and molecular modelling applications of YASARA software (v21.8.27 as per the procedural guidelines provided in the earlier reports[42,59,60]). For performing energy minimization experiments in explicit solvents such as water and HFP (1,1,1,3,3,3-hexafluoro-2-propanol), the simulation box was created around the molecular structure and box was filled with explicit solvent molecules randomly as per their density parameters at 25°C (solvent density equal to 0.997 g/ml and 1.57 g/ml respectively, for water and HFP).[61] The maximum sum of all bumps per solvent molecule was set equal to 1.0 Å. The 3D molecular geometry of SN peptide and its further energy minimized conformation in HFP solvent is shown in supplemental information (Figure S5). The generated SN peptide structure was used for predicting the possibly peptide-peptide interaction model using VINA docking method.

Fourier transform infrared spectroscopy (FT-IR)

Fourier transform infrared spectra were recorded using an IRTracer-100 FT-IR spectrometer (Shimadzu) with a Deuterated Lanthanum α-Alanine doped TriGlycine Sulphate (DLaTGS) detector. The peptide self-assembled solutions were deposited on a CaF_2 window and dried under a vacuum. The peptide deposits were suspended with D_2O and dried to form thin films. The re-suspension procedure was repeated twice to ensure maximal hydrogen-to-deuterium exchange. The measurements were taken using 4 cm^{-1} resolutions and an average of 2000 scans. The transmittance minimal values were determined using the Lab solutions IR analysis program (IR Tracer).

UV-Vis spectroscopy

UV-Vis absorption spectra of the synthesized peptides were recorded using a UV-Vis spectrophotometer (Agilent, Cary 60, Double beam UV-Vis absorption spectrometer).

Fluorescence spectroscopy

Steady-state fluorescence measurements were performed at RT using a fluorescence spectrometer (Edinburg Instruments, FLS-1000). The emission spectra of the synthesized peptides were recorded in different solvent media using appropriate excitation wavelengths. For the drug encapsulation and drug release studies, the fluorescence spectra were recorded from 500 to 750 nm (λ_{Ext} = 490 nm). For quantitative analysis, emission intensity at 590 nm was monitored.

Dynamic light scattering (DLS) analysis

Dynamic light scattering (DLS) analysis of the hollow spherical assemblies formed by SN was performed using a Nano-zeta sizer (Horiba Sz-100), and these measurements were performed at RT, 25°C.

Drug loading and drug release of SN-Based self-assembled superstructures

The incorporation of Doxorubicin (Dox) was conducted during the self-assembly of SN. Dox at a concentration of 10^{-1} mol L^{-1} (dissolved in water) was added to SN (dissolved in HFP at 100 mg mL^{-1} concentration) to the desired final concentration (2.0 mg mL^{-1} effective concentration). Then, the mixture was left overnight to undergo spontaneous encapsulation of the drug molecule within the SN-based hollow spherical structures in 100% aqueous solvent medium. Following conjugation, samples were prepared by drop-casting 25μL of the conjugate mixture on the glass coverslip and dried in air. The remaining solvent was left drying overnight at RT under vacuum. Then, the assemblies were washed carefully with ultrapure water several times to eliminate the residual or free Dox and dried at RT. The drug-incorporated self-assemblies were prepared by the above-mentioned protocol and dispersed in PBS (10 mM NaCl pH = 7.4, 150 mM). After that, this suspension (2 mL) was transferred into a dialysis bag (MWCO 3 kDa), and the bag was dipped in 40 mL of PBS at RT. The emission intensity of the buffer solution outside the dialysis bag was measured at different time intervals for 30 hrs. The volume of the solution was kept constant by

adding 1 mL of the original PBS solution after each measurement. The emission intensities were measured at RT using a fluorescence spectrophotometer. The emission spectra were recorded from 500 nm to 750 nm for the % drug release vs. time plot (λ_{Ext} = 490 nm and λ_{Mon} = 590 nm).

Drug-encapsulation efficiency (EE) and loading capacity (LC) calculation

SN-Dox conjugate was prepared as reported above and left to precipitate overnight. The aqueous medium was decanted and the emission intensity at the desired wavelength was measured. The drug-encapsulation efficiency (EE), which is correlated with the concentration of the drug not incorporated or the free unentrapped drug molecule, can be expressed by Equation1.[62]

$$EE = \frac{Actual\ concentration\ of\ the\ drug\ incorporated\ in\ nanoparticles}{Concentration\ of\ the\ theory\ \ amount\ of\ drug\ loaded\ in\ Nanoparticles} \times 100\% \quad \text{(Equation 1)}$$

$$EE = \frac{Emission\ intensity\ of\ the\ drug\ incorporated\ in\ nanoparticles}{Emission\ intensity\ of\ the\ theory\ \ amount\ of\ drug\ loaded\ in\ Nanoparticles} \times 100\% \quad \text{(Equation 2)}$$

$$EE = \frac{Emission\ intensity\ of\ the\ theory\ amount\ of\ drug\ loaded\text{-}Emission\ intensity\ of\ the\ drug\ not\ incorporated}{Emission\ intensity\ of\ the\ theory\ \ amount\ of\ drug\ loaded\ in\ Nanoparticles} \times 100\% \quad \text{(Equation 3)}$$

As the concentration of the drug is directly proportional to the emission intensity, Equation 2, the emission of the drug incorporated in nanoparticles is equal to the total emission subtracted by the emission intensity of the drug not incorporated; EE can be calculated using Equation 3.

The loading capacity (w/w %LC) can be calculated using the following expression:

$$C = \frac{Amount\ of\ the\ Entrapped\ drug}{Nanoparticle\ \ weight} \times 100\%$$

The molecular weight of the Dox = 543.52 g/mol. For the drug encapsulation study final volume of the resultant solution is 1 mL and the final effective concentration of the SN is 2 mg mL^{-1}. The concentration of the fluorescent drug (Dox) loaded is 10^{-3} mol L^{-1}. The drug encapsulation efficiency calculated for the SN based hollow spherical assembly is 68.72%.

The amount of the entrapped drug by the SN based spherical assembly is

0.543 × EE = 0.543 × 68.72% = 0.373 mg.

LC= (0.373/2.0) × 100% = 18.65%

In vitro drug release studies

In order to investigate the effect of glutathione (GSH) on the Dox-loaded hollow spherical assembly, a final GSH concentration of 0-10mM was maintained in SN-Dox suspension and continuously stirred at RT for 30 h. At predetermined time intervals, fluorescence intensities were measured using a fluorescence spectrophotometer (Edinburgh Instruments FLS 100). The emission spectra were recorded from 500 nm to 750 nm for the % drug release vs. time plot (λ_{Ext} = 490 nm and λ_{Mon} = 590 nm). The *in vitro* drug release experiments were performed in triplicate.

MTT assay

The MTT reduction assay was applied to evaluate the cellular toxicity of the synthesized compounds. To examine how the SN and SN-Dox compounds affect cell growth and proliferation, we exposed various cell lines, including HEK293, AC16, MCF7, and MDAMB231, to different concentrations of the compounds for 40 h. After seeding cells at a density of 6 × 10^4 cells per well in a 96-well plate, they were incubated in a CO_2 incubator at 37°C with 5% carbon dioxide. The culture medium used consisted of DMEM supplemented with 10% FCS (Gibco). Following a 24 hrs period, the culture medium was replaced, and the cells were then incubated using a culture medium devoid of phenol red with different concentrations of the synthesized compounds for an additional 40 hrs. 0.5 mg/mL solution of MTT (Sigma) was introduced to each well, and the cells underwent a 3 hrs incubation. After the incubation period, 150 μL of DMSO was added to each well to solubilize the formazan crystals. Finally, a plate reader from Biotek Instruments was used to measure the optical density (OD) at a wavelength of 570 nm.[64]

Fluorometric analysis

A density of 3 × 10^5 cells of HEK293 and AC16 cell lines were seeded in 35 mm dishes having DMEM medium supplemented with 10% FCS and allowed for a 30 hrs incubation period. Then different concentrations of the SN and SN-Dox compounds were treated, and the cells were kept for an additional 24 hrs of incubation. Subsequently, the cells were harvested, washed with chilled PBS, and then lysed in PBS supplemented with 1% Tween 20. The cell lysates were centrifuged, and with an excitation wavelength of 560 nm and an emission wavelength of 633 nm, the fluorescence level of the collected supernatant was evaluated.[64]

Immunofluorescence study

Cover slips were placed in six-well plates and MCF7 cells were grown on them using DMEM enriched with 10% FCS. The treatment of SN and SN-Dox compounds at a concentration of 100 nM in DMEM was done after a 30 hrs incubation period. Following an 8 hrs incubation time with the synthesized compounds, the cells underwent three consecutive 5-minute rinses with a chilled PBS solution. Next, the cells were fixed at room temperature for 10 minutes using 4% paraformaldehyde and subsequently washed twice with cold PBS. The cells were then mounted with Vectashield mounting media (Invitrogen) and subjected for the examination using fluorescence microscopy (Optika B-100FL HBO, Italy) to facilitate the visualization of the labeled fluorescence.[65]

ROS generation study

The cell-permeable oxidation-sensitive probe, CM-H2DCFDA was used to examine the intracellular levels of reactive oxygen species (ROS). Dox and SN-Dox treatment at a concentration of 100 nM was given to the MCF7 or MDAMB231 cells for 24 hrs. The cells were then detached through scraping after the incubation period, collected using centrifugation, and consequently washed twice for 5 minutes each with chilled PBS. Following that, the cells were resuspended in PBS and underwent a 20-minute incubation with CM-H2DCFDA (5 μM) in the dark at 37°C. Next, using cold PBS the cells were again washed and then lysed using PBS having 1% Tween 20. At an excitation wavelength of 480 nm and an emission wavelength of 530 nm, the fluorescence of dichlorofluorescein (DCF) was examined to evaluate the generation of intracellular ROS levels.[65]

Measurement of mitochondrial membrane potential

The assessment of mitochondrial membrane potential (MMP ψM) entailed observing the interaction between the fluorescent dye JC-1 (5,5′,6,6′-tetrachloro-1,1′,3,3′-tetraethyl benzimidazolylcarbo cyanine iodide) and mitochondria. MCF7 and MDAMB231 cells were first cultured in a DMEM medium having 10% FCS. The cells were then incubated for duration of 30 hrs with the treatment of Dox and SN-Dox. Following the incubation period, the cells were harvested for the measurement of the levels of reactive oxygen species (ROS). Cell lysates were subjected to incubation with continuous shaking, with JC-1 (2.5 μg/mL) in a PBS solution at 37°C for around 30–35 minutes. Afterward, the cells underwent three 5-minute washes with cold PBS and were subsequently resuspended in PBS. The ratio of fluorescence intensity at 590 nm to 530 nm was measured to evaluate the mitochondrial membrane potential (MMP ψM).[66]

Apoptosis assay

The quantification of the occurrence of apoptosis in MCF7 and MDAMB231 cancer cells treated with Dox (positive control) and SN-Dox was carried out using the Roche cell death detection kit. An ELISA kit was used for the measurement of the cytoplasmic histone-associated DNA fragments. The findings are displayed as the fold increase in the enrichment factor of cytoplasmic nucleosomes.[67]

DNA fragmentation assay

A chromatin fragmentation assay was used to evaluate the apoptosis. MCF7 cells were seeded at a density of 1×10^6 cells in 6 well plates and subsequently, the cells were exposed to SN, Dox, or SN-Dox for 30 hrs. Following the incubation period, the cells were washed using cold PBS and lysed at room temperature using a buffer with 0.5% Triton X-100, 15 mM EDTA & 20 mM Tris HCl and the lysate fraction containing DNA extracted in phenol/chloroform/isoamyl alcohol (25:24:1) was further incubated with RNase (0.1 mg/mL) and proteinase K ($1 mgmL^{-1}$) for 1 hr. The precipitation of DNA was done from the upper aqueous phase by incubating it overnight at −20°C with 0.1 volume of 3 M sodium acetate (pH 5.2) and 3 volumes of absolute alcohol. The pellet found through centrifugation was then washed using 70% ethanol, air dried and finally it was dissolved in 50 μL TE buffer (10 mM Tris, 1 mM EDTA, pH 8.0). The isolated DNA was separated through electrophoresis on a 2% agarose gel and visualized following staining with ethidium bromide.[13]

Immunoblotting

Following exposure to liquid nitrogen for rapid freezing, the treated cells were then lysed in a RIPA buffer (Abcam) containing pre-mixed protease and phosphatase inhibitors. The cell lysates were prepared and quantification was done with a similar procedure as previously conducted. 20 μg of each protein sample was subjected to SDS-PAGE for the separation and subsequently transferred onto nitrocellulose membranes. After the completion of the transfer, the membranes were washed once by with 1X TBST and then blocked in a 3% BSA solution in 1X TBST for 1 hr. The membranes were then immunoblotted with the suitable primary antibodies and left overnight for incubation at 4°C temperature. Next day after washing the immunoblots with 1X TBST thrice for 10 min each, the immunoblots were then incubated with horseradish peroxidase labelled secondary antibodies for 1 hr. After rinsing the immunoblots with 1X TBST, the detection of immunoreactivity was done by employing chemiluminescence. Image J software (NIH) was used for the quantification of the densitometry of western blots. β-Actin was used for the normalization of the protein expression levels and represented as a ratio comparative to the control conditions for all experiments.[68]

QUANTIFICATION AND STATISTICAL ANALYSIS

Student's *t* test or one- or two-way ANOVA was used to all the data analysis with the Bonferroni post hoc interpretation. Statistical analyses were done through GraphPad Prism software (San Diego, CA, USA), the values are shown as means ± SEM and the results were considered significantly different at $p < 0.05$.